TOPICS OF PARTICLE PHYSICS IN THE VERY EARLY UNIVERSE

MICHELA D'ONOFRIO

Department of Physical Sciences
Faculty of Science
University of Helsinki

ACADEMIC DISSERTATION

To be presented for public criticism
on 15th August 2014, at 12 o'clock,
in Auditorium D101, Physicum, Kumpulan Kampus.

August 2014

Supervisors:

Prof. Kari Rummukainen
University of Helsinki

Prof. Anders Tranberg
University of Stavanger

Reviewers:

Prof. Mikko Laine
University of Bern

Prof. Gert Aarts
Swansea University

Opponent:

Prof. Dietrich Bödeker
University of Bielefeld

Report Series in Physics HU-P-D218
ISSN 0356-0961
ISBN 978-951-51-0083-2 (printed version)
ISBN 978-951-51-0084-9 (electronic version)
http://ethesis.helsinki.fi
Unigrafia

Helsinki 2014

LIST OF PUBLICATIONS

Paper I: Electrically charged curvaton
M. D'Onofrio, R. N. Lerner and A. Rajantie,
JCAP **1210** (2012) 004 [arXiv:1207.1063].

Paper II: The Sphaleron Rate through the Electroweak Cross-over
M. D'Onofrio, K. Rummukainen and A. Tranberg,
JHEP **1208** (2012) 123 [arXiv:1207.0685].

Paper III: The Sphaleron Rate in the Minimal Standard Model
M. D'Onofrio, K. Rummukainen and A. Tranberg,
accepted for publication in PRL [arXiv:1404.3565].

Paper IV: Renormalization of Null Wilson Lines in EQCD
M. D'Onofrio, A. Kurkela and G. D. Moore,
JHEP **1403** (2014) 125 [arXiv:1401.7951].

AUTHOR'S CONTRIBUTION

In **Paper I** the author contributed to the development of the model, performed analytical calculations and the determination of constraints on the parameter space. In both **Papers II** and **III** the author carried out the numerical simulations, obtained data and plots and was active in discussing the results. For **Paper IV** the author contributed to the calculations.

ACKNOWLEDGEMENTS

First of all I would like to thank my supervisors, Kari Rummukainen and Anders Tranberg. Kari has always been helpful and available, providing me with excellent guidance and expertise. He has been supervising me since my Master's thesis and encouraged me to undertake the doctoral program. Anders has also been very supportive and available for discussion, providing knowledge, great didactic skills and invaluable pieces of advice.

I'm indebted to the pre-reviewers of the initial draft of my thesis, Mikko Laine and Gert Aarts, for accurate and sensible comments, which greatly improved the quality of my thesis. I'm grateful to Dietrich Bödeker for having accepted to be my opponent. David Weir did a great job carefully proofreading my thesis with the limited amount of time available.

I would like to thank the Magnus Ehrnrooth Foundation for financial support both for my doctoral studies and for conference travels. I acknowledge also partial support from Jyväskylä University for the conference trip to Australia and from Kari Enqvist's project for the conference in Lecce.

I'm indebted to Guy Moore, Aleksi Kurkela and Jacopo Ghiglieri for hospitality and collaboration during the four months I've spent at McGill University, Montreal, in the autumn 2012. I've learnt a great deal from them and I'm grateful for the opportunity given to me. Two precious people made my stay there memorable and unique: Brandee Diner and Arnaud Lepage-Jutier. I'm deeply grateful to both.

I've spent two months at the University of Geneva, partially supported by Ruth Durrer, whom I warmly thank for giving me this opportunity and for being a great host.

I'm thankful to all the people who invited me for longer or shorter visits to their universities. Anders hosted me for a month at Niels Bohr Institute, Copenhagen, partially covering my expenses. Arttu Rajantie supported my visit to Imperial College, London, for the start of our curvaton project. For the latter, I'd also like to thank Rose Lerner for collaboration and help in introducing me to the new subject. Aleksi Vuorinen invited

me to Bielefeld and Manu Paranjape to the Université de Montréal.

From the University of Helsinki I would like to thank Keijo Kajantie, my academic grandfather, great physicist and good friend. Mikko Sainio deserves to be praised a lot for his attentive work and for creating a cheerful atmosphere at the department. I had the pleasure to get to know Anca Tureanu both as my teacher and my colleague, and I had the chance to appreciate her kindness and desire to help.

I was lucky enough to share my path with other fellow Ph.D. students and postdocs which made the department a happier place and the winters shorter. My first thanks goes to Lotta Mether, who has been my comfort in the hard times and joy in the good ones. I thank Anne Mykkänen for friendship and all the great time spent together. I also want to thank Noora Partamies, Aleksi Vuorinen, Dani Figueroa, Shaun Hotchkiss, David Weir, Aneliya Karadzhinova, Erik Brücken, Janne Alanen, Anna-Stiina and Ville Suur-Uski for great moments of fun.
From the Italian community I'd like to thank Francesco Devoto, Giacomo Fedi, Viola Allevato, Marco Panero, Stefano Di Chiara, Roshan Foadi, Stefano Magni, Mahdi Biagioli and Taru Keskinen, for fun, support and great food.

I'm thankful for all the people I've met at conferences, for great discussions. In particular I'm grateful to Fabio Bernardoni for his friendship and support. I also acknowledge recurrent delightful conversations with Chris Byrnes, Isaac Stern and Dominika Konikowska around Europe.

My friends which are far away but close to my heart deserve my deepest thank you for their affection and support: Caterina, Matteo, Massimiliano, Elena, Sara, Cristina and Flavia. I want to thank my French friend Morgan Lethuillier, for interesting days at the office and playful afternoons.

I want to thank Ville Merilä for encouragement, support and advice.

A heartfelt thanks goes to Heikki Seppälä: without you this thesis would not be here.

I would like to express my profound gratitude to my family, for their unique love, caring and support I couldn't have made without. Thank you so much for accepting and appreciating my path.

Last but by no means least, I'm deeply grateful for having a wonderful partner by my side. Thank you, Roberto, for believing in me, encouraging and understanding.

In the beginning the Universe was created.
This has made a lot of people very angry
and been widely regarded as a bad move.

D. Adams

CONTENTS

1

INTRODUCTION

1.1 THE EARLY UNIVERSE

The true nature of the Universe at its birth is a highly speculative matter. Extrapolating from our current knowledge of the Universe, we can deduce temperature and energy density were very large at the time of its birth. It is believed there was a time when the Universe had infinite density and negligible radius, a time known as the Big Bang, and when the laws of physics as we know them broke down. This is often referred to as the initial singularity.

Presumably, at very early times, all four fundamental forces were unified at the Planck scale, at about 10^{19} GeV, with gravity decoupling earlier from the other forces, resulting in the so-called Grand Unification epoch, at around 10^{15} GeV. This hypothesis is motivated by the unification of the running coupling constants of strong and electroweak forces when extrapolated to high energies.

The GUT scale is typically also associated with a period of inflation: it has been suggested that the Universe underwent an extremely rapid exponential expansion, during which its volume grew hugely, probably at least for about 60 e-folds, the time in which an exponentially growing quantity increases by a factor of e. Inflation was supposedly driven by an unknown inflaton field ϕ and left a cold and diluted Universe at its end. However, the inflaton must have decayed at the end of inflation into hot radiation, thus "reheating" the Universe and restoring the hot conditions of the Big Bang. At this point the Universe was a primordial soup of elementary particles.

At these high energies, however, all particles of the Standard Model were massless. Only after the electroweak phase transition, which broke the $SU(2) \times U(1)_Y$ into $U(1)_{em}$, did particles receive their masses through the Higgs mechanism. In the Standard Model framework, the electroweak phase transition is actually a smooth

crossover, which took place at a temperature of T_c ~150 GeV, 2×10^{-11} s after the Big Bang. It has also been suggested that baryogenesis might have occurred at the same time as the electroweak symmetry breaking.

At this point all the four forces were distinct, but the Universe was still too hot for the formation of hadrons from quarks. The quark epoch lasted between 10^{-12} s and 10^{-6} s after the Big Bang.

With the expansion and cooling of the Universe, the QCD phase transition took place at a temperature of $T_c \sim 150$ MeV, 20μs after the Big Bang. Below this scale, QCD is strongly coupled, while above it quarks and gluons are asymptotically free, forming the quark-gluon plasma (QGP). At the transition, quark energies decreased and quarks went from being free to confined into colorless bound states. Quarks and gluons formed baryons and mesons. The lightest baryons are the nucleons: the proton and the neutron, while the lightest mesons are the pions: $\pi^{\pm}, \pi^0$. Baryons are fermions, while mesons are bosons.

Before the Universe was one second old, photons were energetic enough to separate protons and neutrons in formed nuclei, with nuclear binding energies being of the order of 1 MeV. This means the Universe was composed of a sea of elementary particles interacting with each other. When the temperature reached the binding energy of light elements ~ 2 MeV, primordial nucleosynthesis started.

The Universe, however, was still opaque. Photons needed to wait until about 378˙000 years later to be able to travel freely without being scattered from electrons. The last scattering surface constitutes the Cosmic Microwave Background Radiation.

For the first ~ 10^5 years after the Big Bang, the Universe was dominated by radiation (photons and neutrinos) in energy density. Eventually matter became dominant as the energy density of radiation evolves as a^{-4} and that of matter as a^{-3}. Matter-radiation equality occurred and the Universe became matter dominated. It is argued that dark matter now dominates the energy density of the Universe.

In this thesis, we will use the $(-,+,+,+)$ convention for the Minkowski metric. In chapter 2 we will work with curved spacetime, in the Friedmann-Robertson-Walker metric

$$ds^2 = -dt^2 + a^2(t)\left[\frac{dr^2}{1-\kappa r^2} + r^2(d\theta^2 + \sin^2\theta d\phi^2)\right], \tag{1}$$

where r, θ and ϕ are spherical coordinates, $a(t)$ is the scale factor which relates physical and comoving distances

$$d_{phys} = a(t)\, d_{com}, \tag{2}$$

and κ is unitless and represents the curvature. For a Universe that is open, infinite and negatively-curved $k < 0$, open, infinite and flat $k = 0$ or closed, finite and positively-

Event	Time	Temperature
Inflation	?	?
Electroweak Phase Transition	2×10^{-11} s	150 GeV
QCD Phase Transition	2×10^{-5} s	150 MeV
Neutrino Decoupling	1 s	1 MeV
Electron-Positron Annihilation	10 s	0.5 MeV
Big Bang Nucleosyntesis	10 min	100 keV
Matter-Radiation Equality	6×10^{4} yr	0.8 eV
Recombination	2-4$\times10^{5}$ yr	0.3 eV
CMB decoupling	4×10^{5} yr	0.2 eV
Reionization	1-4$\times10^{5}$ yr	2-7 meV
Present	13.7×10^{9} yr	0.2 meV

Table 1: Short history of the early Universe. The values are to be taken as orders of magnitude, rather than accurate estimates.

curved $k > 0$. In this metric we can find an analytic solution to Einstein's equations

$$G_{\mu\nu} + g_{\mu\nu}\Lambda = 8\pi T_{\mu\nu} \tag{3}$$

where

$$G_{\mu\nu} = R_{\mu\nu} - \frac{1}{2}R g_{\mu\nu}$$

is the Einstein tensor with Ricci curvature tensor $R_{\mu\nu}$ and Ricci scalar R, Λ the cosmological constant and $T_{\mu\nu}$ the stress-energy tensor.

The solutions to eq. (3) are obtained with the assumption that the energy tensor be isotropic and homogeneous, and they are the Friedmann equations:

$$\left(\frac{\dot{a}}{a}\right)^2 = \frac{4\pi G}{3}\rho - \frac{k}{a^2} + \frac{\Lambda}{3} \tag{4}$$

$$\frac{\ddot{a}}{a} = -\frac{4\pi G}{3}(\rho + 3p) + \frac{\Lambda}{3} \tag{5}$$

where ρ is the energy density and p the pressure. The first equation is obtained from the 00-component of Einstein's equations, and the second one from their trace. The dependence of the scale factor on time changes according to the content of the Universe, more precisely,

$$a(t) = \left(\frac{3H_0}{2}\right)^{2/3} t^{2/3} \qquad \text{matter- dominated} \tag{6}$$

$$a(t) = (2H_0)^{1/2}\, t^{1/2}. \qquad \text{radiation-dominated} \tag{7}$$

where $H = \dot{a}/a$ is the Hubble parameter and the 0-subscript indicates the current value of a quantity varying in time.

1.2 THE STRUCTURE OF THIS THESIS

In this thesis we examine three different processes of high-energy particle physics. We will present them in the same order as they occurred in the early Universe, see the first three entries in table 1. In chapter 2, a model for inflation is presented, in which the auxiliary curvaton field is assumed to possess a U(1) hypercharge. The consequences of this are explored and the viable regions of phase space determined.
Then, in chapter 3, a mechanism of net baryon-number production is investigated. In the Minimal Standard Model, there exists a process intrinsic to the nature of the electroweak theory, sphaleron transition, which naturally violates baryon-number conservation. The characteristics of the transition are studied, and parameters such as critical temperature, Higgs field expectation value and sphaleron rate are determined.
In chapter 4, we approach the QCD phase transition by studying the quark-gluon plasma existing in the symmetric phase. This same plasma can be recreated in high-momentum particle collisions in accelerators, and can be probed thanks to the emitted particle jets which traverse it and lose energy. In the appendix, the research papers associated with this thesis are attached.

2

INFLATION WITH A CHARGED CURVATON

2.1 INFLATION

The inflationary paradigm was originally introduced in 1981 by Guth [1] to solve three problems of Standard Cosmology: the flatness and the horizon problems as well as the issue of unwanted relics.

THE FLATNESS PROBLEM. The first of Friedmann equations, eq. (4), can be rewritten as

$$H^2 = \frac{\rho}{3M_{Pl}^2} - \frac{k}{a^2}, \tag{8}$$

where $M_{Pl} = \sqrt{\hbar c/8\pi G}$ is the Planck mass, and then in terms of the critical energy density $\Omega \equiv \rho/\rho_c$, with $\rho_{cr} = 3m_{Pl}^2 H^2$, to obtain

$$\Omega_k \equiv \Omega - 1 = \frac{k}{a^2 H^2}. \tag{9}$$

As the Universe is nearly flat ($k = 0$, $\rho \approx \rho_{cr}$), Ω is approximatively 1. From recent measurements [2], we know that $\Omega_k \sim 0.07$. From eq. (9) it follows that, if a increases and H is basically constant, Ω_k has been increasing all the time. If now Ω is so close to 1, it must have wandered away from an early-Universe value even closer to the critical value. The fine tuning of the primordial H (below Planck scale) should be as accurate as 10^{-55} [1].

Inflation solves this problem in that the great acceleration $\ddot{a} > 0$ would have increased $\dot{a}$ hugely, thus eliminating any deviation from flatness. After inflation, $\dot{a}$ decreased from the inflation value, making Ω_k grow.

THE HORIZON PROBLEM. The cosmic microwave background radiation is homogeneous and isotropic to a level of one part in 10^{-5} in temperature perturbations, still it consists of patches which cannot have been in causal contact with each other.

The solution may come from inflation, during which the formerly connected regions of space moved far away from each other, in our horizon and beyond it. If we calculate the maximum distance any particle could have ever travelled, the comoving horizon distance (scaled with $a(t)$), we get the conformal time

$$\eta(t_0) = \int_0^{t_0} \frac{dt}{a(t)}, \tag{10}$$

where we have omitted c which is 1 by convention. Comparing the size of the horizon today and at Planck time, we get a factor of 10^{26}, which means the Universe today has about 10^{78} regions which were causally disconnected at Planck time. If we express eq. (10) in terms of the scale factor a,

$$\eta(a_0) = \int_0^{a_0} \frac{d\ln a}{aH}, \tag{11}$$

we get the explicit dependence of η on the comoving Hubble radius $\mathscr{H}^{-1} = 1/aH$. This gives the maximum distance between two causally-connected points.

For the Universe to be so homogeneous, regions of space now far from each other must have been once in causal contact. This means the comoving Hubble radius was once bigger and then decreased in size. As H was nearly constant while a was growing, the only way for this to happen is to have $\ddot{a} > 0$, a period of accelerated expansion: inflation.

THE UNWANTED RELICS. The early Universe underwent a series of symmetry-breaking transitions, which should have resulted in plenty of topological defects formed at the boundaries between the old and the new phases. In particular, it has been estimated [3] that the number density of magnetic monopoles should be as high as the one of protons and neutrons. However, these have not been observed, and, moreover, their huge mass would have prevented the Universe from expanding. The inflationary model solves this puzzle by diluting the monopoles during the exponentially accelerated expansion.

2.1.1 *The inflationary model*

Inflation was a period of time in the early Universe characterized by a rapid expansion, during which the scale factor was accelerating

$$\ddot{a} > 0, \tag{12}$$

or, in terms of Hubble length

$$0 < \ddot{a} = \frac{d}{dt}(\dot{a}) = \frac{d}{dt}(aH). \tag{13}$$

While the Universe is accelerating, the comoving Hubble length $\mathscr{H}^{-1} = 1/aH$ was decreasing with time, therefore making the observable Universe smaller during inflation.

By imposing $\ddot{a}/a > 0$ in the second Friedmann equation (5), we get

$$\rho + 3P < 0 \tag{14}$$

which implies $P < 0$, as the energy density is always positive. In order to have inflation, there must be a field driving it. Fields with negative pressure are scalar fields, and the one driving inflation is called the inflaton. Solving eq. (5) for the conditions of eqs. (12) and (14), we obtain the solution for the scale factor

$$a(t) \sim e^{Ht}, \tag{15}$$

which is indeed exponentially growing with time.

The huge expansion virtually cooled down the temperature to zero. When inflation ended, the Universe is reheated to high temperature and the hot Big Bang could take place.

2.1.2 *Inflation ends*

In the first theories of inflation, which were supposed to occur in the context of a GUT phase transition, bubbles of the broken phase form, bringing regions of space from a false vacuum to the true vacuum, as shown in the first of fig. 1. The transition happens through tunneling. Then the bubbles would grow, collide and release the energy produced in wall collisions (latent heat). However, as the Universe is expanding exponentially, the bubbles would never collide, consequently not filling the whole Universe with the new phase. In this way inflation would continue forever.

The need for a different kind of potential brought the development of a different method for symmetry breaking, through higher-order corrections to the potential, the Coleman-Weinberg corrections [8], which are of the form

$$\Delta V = \frac{3g^4}{64\pi^2}\phi^4 \ln\frac{\phi}{\langle\phi\rangle} \tag{16}$$

where g is the coupling constant, ϕ is the field generating the potential and $\langle\phi\rangle$ its vev. The potential now depends on the temperature of the Universe, as shown in fig. 1.

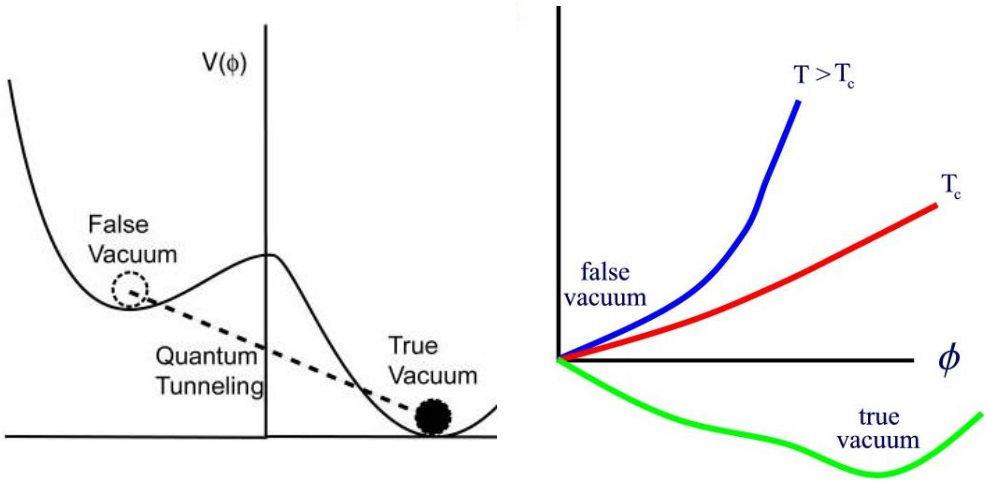

Figure 1: Different types of potential assumed to drive inflation. In the left-hand figure, the classical symmetry-breaking potential for GUT inflation. In the right-hand figure, the potential is modified to be temperature-dependent and allow the inflation to end (Coleman-Weinberg potential). From [4].

At high temperatures, the true vacuum and the symmetric phase coincide. When the temperature decreases, a second vacuum forms at a field value, where the gauge symmetry is broken. The second vacuum is a true vacuum and the field starts to slowly roll towards it from the symmetric false vacuum. In this scenario inflation ends when the field has reached the true vacuum.

2.1.3 *Curvature perturbations*

Perturbations in the energy density of the early Universe ($T \sim 1$ MeV) are called primordial perturbations, and provide the initial conditions for the subsequent evolution and structure formation. A powerful tool to study primordial perturbations is the separate-universe approximation. This is based on the assumption that the Universe be isotropic and smooth on a comoving distance scale k^{-1}. In this way, the Universe evolves at each point as an unperturbed universe, providing the background upon which perturbations evolve.

Consequently, we can define a quantity q as being composed by a component smoothed over a sphere and perturbations to the average value

$$q(r,x,t) = q(t) + \delta q(r,x,t), \tag{17}$$

where r is the comoving radius of the sphere and (x,t) the coordinates of the center of the sphere.

Now let us examine the correlation between the different Fourier components of δq_k. If there is no correlation between such components, the probability distribution of $\delta q(x)$ is Gaussian. If there exists correlation, it is seen in the probability distribution as skewness, and the perturbation is said to be non- Gaussian.

Non-Gaussianity is a measure of inflaton interactions (determined by its 3-point functions and higher). The non-Gaussianity parameter f_{NL} is defined in terms of the (gauge-invariant) comoving curvature perturbations as

$$\mathcal{R} = \mathcal{R}_G + \frac{3}{5} f_{NL} \mathcal{R}_G^2 \tag{18}$$

A simple model of primordial non-Gaussianity is local non-Gaussianity defined by a Taylor expansion of the curvature perturbation around the Gaussian part $\mathcal{R}_G$.

The root mean square of the density perturbation $\delta\rho(r,x)$ evaluated at horizon entry does not depend on the smoothing scale. This means that density perturbations are scale invariant. Small deviations from invariance constitute are characterized by the spectral index $n(k)$, defined by

$$n - 1 \equiv \frac{d \ln \mathcal{P}_\zeta(k)}{d \ln k}, \tag{19}$$

with $\mathcal{P}_\zeta(k)$ the spectrum of the curvature perturbation.

The curvature perturbation ζ is defined through

$$a(\mathbf{x}, t) \equiv a(t) e^{\zeta(\mathbf{x},t)}, \tag{20}$$

where $a(\mathbf{x}, t)$ is a locally-defined scale factor, while $a(t)$ is the background one.

If a cosmological quantity is a unique function of its energy density, it satisfies the so-called adiabatic condition. Departures from the adiabatic condition are called isocurvature density perturbations, and defined as

$$S_c = \delta_c - \frac{3}{4}\delta_r \tag{21}$$

$$S_B = \delta_B - \frac{3}{4}\delta_r \tag{22}$$

$$S_\nu = \delta_\nu - \frac{3}{4}\delta_r, \tag{23}$$

where the $\delta_i \equiv \delta\rho_i/\rho_i$ are the energy density contrasts, the subscripts c, B, ν mean respectively dark matter, baryons, neutrinos and $\rho_r = \rho_\nu \rho_\gamma$ is the energy density of radiation.

2.1.4 *Curvaton model*

In the standard inflaton scenario, curvature perturbations originate during inflation, from the quantum fluctuations of the slowly-rolling inflaton field. As cosmological scales leave the horizon, quantum fluctuations are converted to classical gaussian perturbations with an almost flat spectrum, generating immediately the curvature perturbation which is constant until the approach of horizon entry.

The assumption that the inflaton produced all of the curvature perturbations is, however, very restricting on the possible models of inflation allowed [5]. In the curvaton paradigm, instead, there is a secondary field, the curvaton σ, which produces curvature perturbations, while the inflaton ϕ drives the expansion. The curvaton is light and subdominant during inflation and gains an isocurvature perturbation. The curvaton starts oscillating during a radiation-dominated era and continues for many Hubble times. After inflation has ended, the energy density of the curvaton grows relative to the background radiation. When the curvaton decays, its isocurvature perturbation is converted to an adiabatic perturbation that can seed the structure in the Universe. The decay of the curvaton happens through parametric resonance, which leads to a period of non-linear dynamics. This is the time at which non-Gaussianity is supposed to be generated.

Even though the curvaton is subdominant during inflation, as its energy density evolves as a^{-3}

$$\rho_\sigma \approx m^2\sigma(t)^2 \approx 0.74\frac{m^{1/2}\sigma_*^2}{t^{3/2}}, \tag{24}$$

where m is the curvaton mass and the subscript $_*$ denotes values at the end of inflation. Radiation energy density decreases proportional to a^{-4}

$$\rho_\gamma = \frac{3M_{Pl}^2H_*^2}{a^4} = \frac{3M_{Pl}^2}{4t^2}, \tag{25}$$

the relative fraction of curvaton energy density $r(t)$

$$r(t) \equiv \frac{3\rho_\sigma(t)}{3\rho_\sigma(t)+4\rho_\gamma(t)} \tag{26}$$

grows with time like

$$a \propto t^{1/2} \tag{27}$$

for a radiation-dominated Universe, see eq. (7), and its energy density contribution (and curvature perturbation) becomes dominant. The 3- and 4-factors in eq. (26) are weighting factors according to the evolution of the curvaton (a^{-3}) and radiation

(a^{-4}), respectively. Eventually, the curvaton decays into Standard Model particles which have the equation of state of radiation, at which point the perturbations in the curvaton become adiabatic. Assuming that this happens instantaneously at time t_{dec}, the amplitude of the curvature perturbation is given by [5]

$$\zeta \approx \frac{r(t_{dec})}{3} \frac{\delta\rho_\sigma}{\rho_\sigma}. \tag{28}$$

This needs to agree with the observed amplitude $\zeta \simeq 10^{-5}$. In the standard curvaton model, in which eq. (24) remains valid until the decay time, this becomes

$$\zeta \approx \frac{r(t_{dec})}{3} \frac{2}{\sigma_*} \delta\sigma_* \approx \frac{H_* r(t_{dec})}{3\pi\sigma_*}. \tag{29}$$

With the same assumption, the non-Gaussianity of the perturbations is given by

$$f_{NL} \approx \frac{5}{4r_{dec}}. \tag{30}$$

Before cosmological scales enter the horizon, the curvaton decays and it is assumed that the produced curvature perturbation remains constant. Quantum fluctuations during inflation are converted into curvature perturbations after curvaton decay [6]. Curvature perturbations are important because they are believed to have seeded the formation of structures in the Universe.

2.2 ELECTRICALLY CHARGED CURVATON

Models of inflation are based on quantum field theory, although generally they describe particles that are not present in the Standard Model of particle physics. However, in order for reheating to take place after inflation, the inflaton needs to couple with some SM field. Therefore it is desirable to link inflationary physics with the Standard Model.

We investigated the possibility of a curvaton charged under a Standard Model gauge group. In addition to the aforementioned argument, there is also the advantage of knowing the couplings of the interaction. This model has therefore fewer parameters compared to other curvaton models. We chose to investigate a U(1) weak hypercharged curvaton, because of the more straightforward physics involved, as well as the potentially interesting curvaton– photon interactions and subsequent curvaton contribution to curvature perturbation.

The inflaton field ϕ is not coupled to the curvaton, and has a quartic potential. The Lagrangian density for the theory is

$$\begin{aligned}\mathscr{L} &= \frac{1}{2}\partial_\mu\phi\,\partial^\mu\phi + \frac{1}{4}\lambda_\phi\phi^4 - \frac{1}{4}F^{\mu\nu}F_{\mu\nu} \\ &\quad -m^2\sigma^\dagger\sigma - \lambda(\sigma^\dagger\sigma)^2 + (D_\mu\sigma)^\dagger(D^\mu\sigma)\end{aligned} \tag{31}$$

where $D_\mu = \partial_\mu - ieA_\mu$ and $F_{\mu\nu} = \partial_\mu A_\nu - \partial_\nu A_\mu$.

2.2.1 *Constraints on the effective potential*

The large value of the curvaton gauge coupling e gives rise to Coleman- Weinberg corrections to the potential, which can have a substantial impact on the parameter space of the model [7]. Assuming that the one-loop corrections are dominated by the gauge coupling e, the effective potential is [8]

$$V_{\rm eff}(\sigma) = m^2|\sigma|^2 + \frac{3e^4}{64\pi^2}|\sigma|^4 \ln\left(\frac{|\sigma|^2}{\mu^2}\right), \tag{32}$$

where the self-coupling constant λ has been absorbed into the definition of the renormalisation scale μ. Therefore, the free parameters are m and μ.

The shape of this potential is shown in fig. 2. For small μ, the U(1) symmetric vacuum $\sigma = 0$ is the only minimum. At larger μ, a second minimum with $\sigma \neq 0$ appears, and when μ is large enough, this symmetry-breaking minimum becomes the true vacuum.

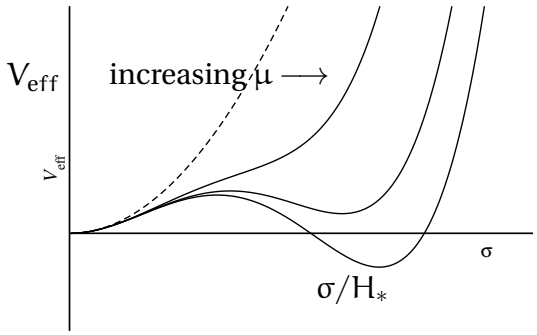

Figure 2: The effective potential $V_{\rm eff}(|\sigma|)$ of the curvaton field. The dashed line shows the quadratic tree-level potential, and the three solid lines show the effective potential for increasing μ, from left to right.

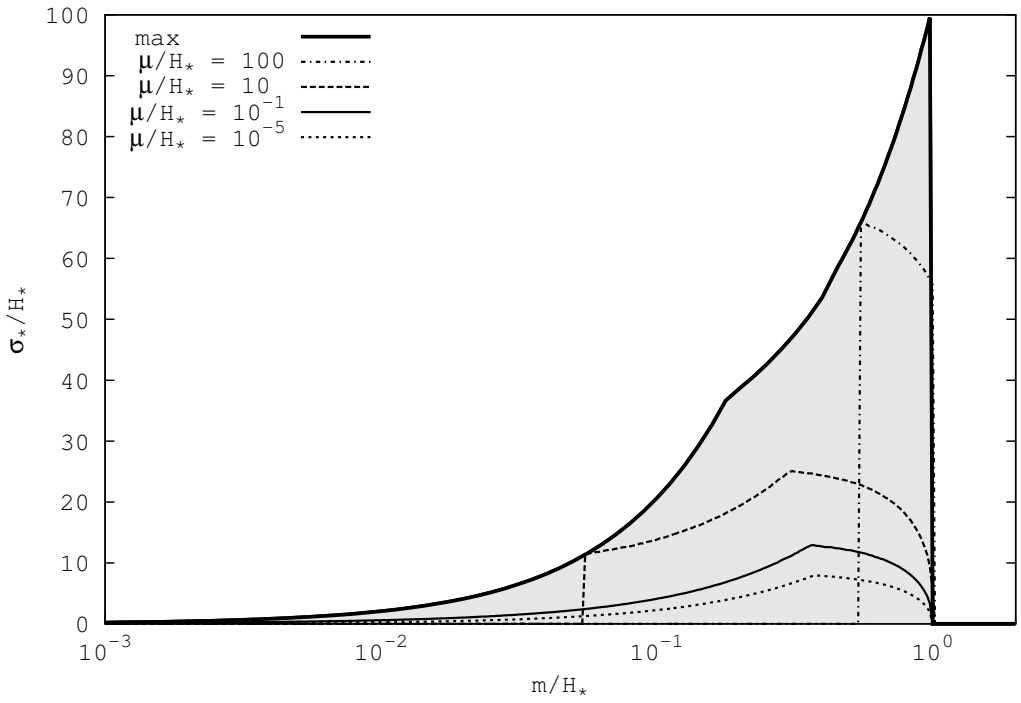

Figure 3: Allowed region (shaded) for a viable curvaton model satisfying conditions 1–3 in the text. Note that these conditions only guarantee the existence of a curvaton, but not that the generated perturbations are compatible with observations. Also shown are the maximum σ_* for various constant μ; vacuum instability rules out large μ and small m. The parameter space is independent of H_*. This is because H_* only determines the subdominance of the curvaton during inflation, which is naturally satisfied provided the other conditions are met. Figure from Paper I.

In order for σ to act as a curvaton field, the effective potential has to satisfy certain conditions:

1. **Vacuum stability:** The symmetric vacuum $\sigma = 0$ has to be the true vacuum, otherwise the Universe would tunnel into the vacuum with $\sigma \neq 0$, which would break the U(1) symmetry spontaneously and make the photon massive.

2. **Shallow potential:** In order to gain a nearly scale-invariant spectrum of perturbations during inflation, the curvaton field has to be light compared to the Hubble rate H_*. This means that its effective mass $m_{\rm eff}$, defined as

$$m_{\rm eff}^2 \equiv V''_{\rm eff}(\sigma_*) \tag{33}$$

has to be less than the Hubble rate H_* during inflation. In addition, the curvaton should be subdominant compared with the inflaton potential because otherwise it would be an inflaton. This means that the effective potential has to satisfy

$$V_{\text{eff}}(\sigma_*) \ll 3M_{\text{Pl}}^2 H_*^2. \tag{34}$$

Both of these conditions, eq. (33) and eq. (34), restrict the height of the effective potential, and also the maximum value of the curvaton field σ_*.

3. **Linearity:** The curvaton has to evolve linearly both during and after inflation. During inflation, we have to make sure that the effective mass (eq. (33)) is light over the whole range of field values present in the observable Universe.

   After inflation, we require that the potential is dominated by the mass term $m^2|\sigma|^2$, so

$$m^2 \gg \left|\frac{3e^4}{64\pi^2}\sigma_*^2 \ln\left(\frac{\sigma_*^2}{\mu^2}\right)\right|. \tag{35}$$

   This implies that the curvaton has the equation of state of matter after inflation, making it easy to study the dynamics. The condition also guarantees that if a metastable second minimum exists, the field is on the left side of the barrier and starts to oscillate around the symmetric minimum.

The effect of these constraints is shown in fig. 3. The regions are highly non-trivial, both on the value of σ_*, and on the mass of the field. The combination of these constraints favors large curvaton mass $m \gtrsim 10^{-2} H_*$, relatively (but not unnaturally) low field values $\sigma_* \lesssim \mathcal{O}(100) H_*$, and $\mu \lesssim \mathcal{O}(100) H_*$. The maximum σ_* for various constant values of μ is also shown, to demonstrate that larger values of σ_* are only possible for larger values of μ.

2.2.2 *Evolution of the curvaton*

During inflation, the inflaton dominates the energy density, but its perturbations are assumed to be negligible. The curvaton field is light (compared to the Hubble rate H_*), and therefore it develops a nearly scale-invariant spectrum of fluctuations, in the same way as the inflaton. After inflation, it is assumed that the inflaton reheats to produce a thermal bath, which becomes the dominant form of energy in the Universe.

As the Universe expands, H decreases, and when $H \lesssim m$, the curvaton begins to oscillate in its potential. From the relevant part of the Lagrangian

$$\mathcal{L}_\sigma = |(i\partial_\mu - eA_\mu)\sigma|^2 - \frac{1}{2}m^2\sigma^\dagger\sigma, \tag{36}$$

the Euler-Lagrange equation for the field σ is

$$\Box\sigma - \frac{\partial V(\sigma)}{\partial \sigma^\dagger} = 0. \tag{37}$$

In curved spacetime, the d'Alembertian has the form

$$\Box\sigma = \frac{1}{\sqrt{-g}} D_\mu (\sqrt{-g} g^{\mu\nu} D_\nu \sigma)$$

Using the FRW metric in eq. (1), $\sqrt{-g} = \sqrt{-\det g_{\mu\nu}} = a^3$, and the temporal gauge $A_0 = 0$ we obtain

$$\Box\sigma = -\ddot{\sigma} - 3H\dot{\sigma} + \frac{ie(\partial_i A_i)\sigma}{a^2} - \frac{e^2 A^2 \sigma}{a^2},$$

where the dot represents time derivative. By ignoring gradient terms, the equation of motion (eq. (37)) becomes

$$\ddot{\sigma} + 3H\dot{\sigma} - \left(\frac{ie\partial_i A_i}{a^2} - \frac{e^2 A^2}{a^2} - \frac{1}{2} m^2 \right) \sigma = 0. \tag{38}$$

The latter is exactly solvable only with non-perturbative methods. For a perturbative approach, we argue that the linear approximation

$$\ddot{\sigma} + 3H\dot{\sigma} + \frac{1}{2} m^2 \sigma = 0 \tag{39}$$

holds, as

$$\frac{ie\partial_i A_i}{a^2} \ll m^2 \qquad \text{and} \qquad \frac{e^2 A^2}{a^2} \ll m^2,$$

assuming A_μ is in the vacuum state during inflation. As we want to solve the equation for σ as a function of time, we insert $H = 1/2t$ for the radiation-dominated case into eq. (39), which eventually becomes

$$2t\ddot{\sigma} + 3t\dot{\sigma} + m^2 \sigma = 0. \tag{40}$$

This is the Bessel's equation, with solution

$$\sigma(t) = \frac{a}{t^{1/4}} J_{1/4}\left(\frac{mt}{\sqrt{2}}\right) + \frac{b}{t^{1/4}} Y_{1/4}\left(\frac{mt}{\sqrt{2}}\right) \tag{41}$$

where J_ν and Y_ν are Bessel's functions of the first and second kind, respectively. In order to find the constants a and b for the initial condition $\sigma(0) = \sigma_*$ we expand Bessel's functions around $x = mt/\sqrt{2} = 0$:

$$\begin{aligned} J_n(x) &= x^n \left[\frac{2^{-n}}{\Gamma(n+1)} - \frac{2^{-n-2}x^2}{(n+1)\Gamma(n+1)} + \ldots \right] \\ Y_n(x) &= x^n \left[-\frac{2^{-n}\cos(n\pi)\Gamma(-n)}{\pi} + \frac{2^{-n-2}\cos(n\pi)\Gamma(-n)x^2}{\pi n + \pi} + \ldots \right] \\ &+ x^{-n} \left[-\frac{2^n\Gamma(n)}{\pi} + \frac{2^{n-2}\Gamma(n)x^2}{\pi - n\pi} + \ldots \right]. \end{aligned}$$

For $n = 1/4$, and inserting the above into eq. (41) we obtain for a and b

$$\begin{aligned} a &= \frac{2^{3/8}\sigma_*}{m^{1/4}}\,\Gamma\left(\frac{5}{4}\right) \\ b &= 0, \end{aligned}$$

which give

$$\sigma(t) = \frac{2^{3/8}\sigma_*}{(mt)^{1/4}}\,\Gamma\left(\frac{5}{4}\right)\,J_{1/4}\left(\frac{mt}{\sqrt{2}}\right). \tag{42}$$

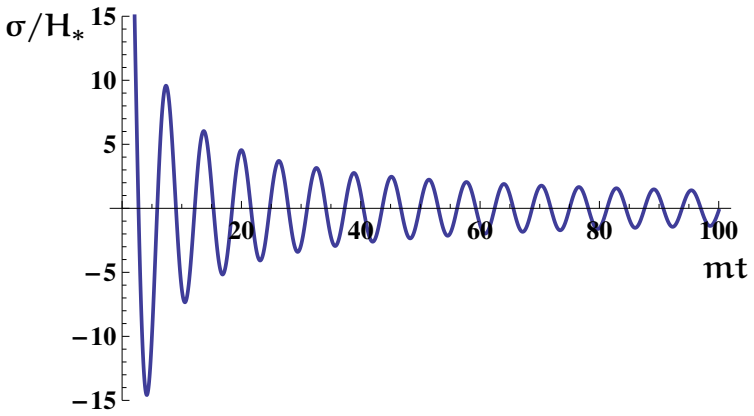

Figure 4: Evolution of a curvaton as a function of time, in curved and expanding spacetime, according to eq. (45), and ignoring all interactions, non-linear terms and backreaction.

ASYMPTOTIC APPROXIMATION FOR THE CURVATON SOLUTION. We can make use of the asymptotic form of J_n for $x \gg |\,\alpha^2 - 1/4\,|$

$$J_n(x) = \sqrt{\frac{2}{\pi x}} \cos\left(x - \frac{\alpha\pi}{2} - \frac{\pi}{4}\right), \tag{43}$$

which, in this case ($\alpha = 1/4$, $x = mt/\sqrt{2}$), becomes

$$J_{1/4}\left(\frac{mt}{\sqrt{2}}\right) = \frac{2^{3/4}}{\pi^{1/2}(mt)^{1/2}} \cos\left(\frac{mt}{\sqrt{2}} - \frac{3}{8}\pi\right). \tag{44}$$

Finally we obtain for the solution of the curvaton

$$\begin{aligned} \sigma(t) &= \frac{2^{9/8}\sigma_*}{\pi^{1/2}(mt)^{3/4}}\,\Gamma\left(\frac{5}{4}\right) \cos\left(\frac{\sqrt{2}mt}{2} - \frac{3}{8}\pi\right) \\ &\approx \frac{\sigma_*}{(mt)^{3/4}} \cos\left(mt - \frac{3\pi}{8}\right), \end{aligned} \tag{45}$$

which is shown in fig. 4.

2.3 EVOLUTION OF THE CURVATON AFTER INFLATION

After the end of inflation, the curvaton is a homogeneous condensate which oscillates in its potential according to eq. (45). Its evolution depends on interactions with other fields, which cause it to decay into curvaton particles.

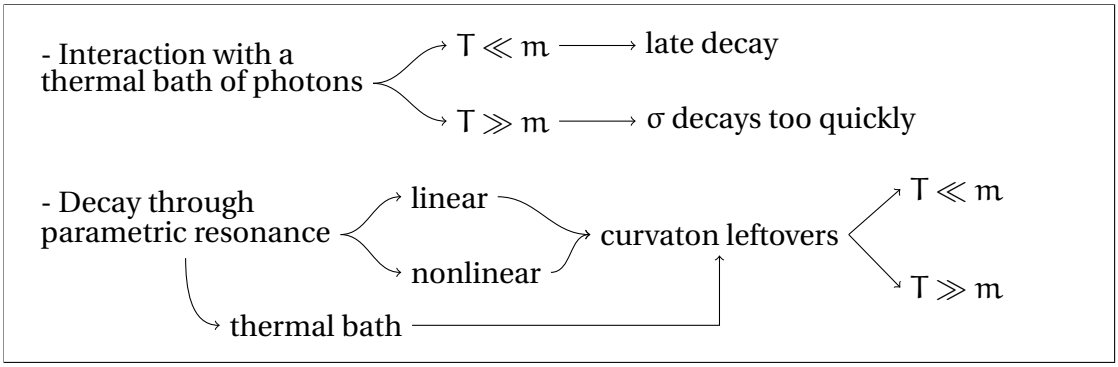

Figure 5: Schematic view of the possible curvaton evolution after inflation.

By curvaton particles, we mean any curvaton field modes with non-zero momentum, and for simplicity we assume that they have a thermal spectrum, so that their behaviour is completely parameterised by their number density and temperature.

The U(1) charge of the curvaton field does not allow a direct Yukawa coupling to Standard Model fermions, but we assume that there is some indirect decay channel, through non-renormalizable interactions or some beyond-the-Standard- Model fields. This allows the curvaton to decay perturbatively into fermions at a slow rate Γ which we treat as a free parameter. At earlier times the curvaton's interactions are dominated by its U(1) gauge coupling, which has two effects: it allows the curvaton condensate to decay non-perturbatively to photons through a parametric resonance; and thermal photons (if present) interact with the curvaton condensate, turning it into curvaton particles.

These processes affect the behaviour and energy density of the curvaton field (and therefore the curvature perturbation ζ) through eq. (29). The curvature perturbation becomes adiabatic when the curvaton either decays or obtains full (chemical and kinetic) thermal equilibrium with the dominant background. To obtain a sufficiently high amplitude of perturbations, it is usually necessary for the curvature perturbation ζ to become adiabatic at very late times. Note that the mechanism of decay can also affect the non-Gaussianity of the model.

From fig. 3 we can see that $\sigma_* \lesssim 100H_*$. Together with eq. (29), this implies that in order to generate the observed amplitude of perturbations the energy fraction in the curvaton field $r_{\rm dec}$ must be less than 10^{-2}. Therefore we can safely assume that the curvaton's contribution to the energy density is subdominant and the background energy density scales like radiation. We find that field values well below the Hubble rate are unnatural, and set a lower limit $\sigma_* > 0.1H_*$.

2.3.1 *Interactions with the thermal bath*

Because the curvaton-photon coupling e is relatively large, the interaction of the curvaton with a thermal bath of photons is significant. The curvaton forms a homogeneous condensate which produces curvaton particles when interacting with photons, with rate

$$\Gamma_{\rm th} \approx 0.03 e^2 T, \tag{46}$$

where the factor was obtained numerically in [9] and T is the temperature of the thermal bath. This interaction, however, does not cause the curvaton particles to decay. The non-perturbative decay of curvatons into photons through parametric resonance is prevented, because this requires a condensate. The subsequent evolution of the curvaton particles depends on the energy scale of both particles and photons.

If the temperature is low ($T \ll m$), then the produced particles are non-relativistic and the equation of state is unchanged compared to that of the oscillating condensate, and may decay at a later time.

If the temperature is high enough ($T \gg m$), the produced curvaton particles are ultrarelativistic and have the equation of state of radiation. In this case, the evolution depends on whether both chemical and kinetic equilibrium are reached. The thermal bath is produced at the end of inflation by the decaying inflaton field, with temperature $T \simeq 0.5\sqrt{M_{Pl}H}$. However, the decay of the inflaton occurs instantaneously and destroys the curvaton condensate. Moreover, the curvaton reaches chemical equilibrium very quickly, before it can produce significant curvature perturbation ζ.

Thus, in order to have a viable model we must impose the requirement that there be almost no photons in the thermal background after inflation. This could occur either (i) if the inflaton decays to a hidden sector, sufficiently decoupled from the Standard Model, or (ii) if the inflaton is blocked from decaying until a sufficiently late time. In the latter case, we require the inflaton to oscillate in a ϕ^4 potential in order for r to grow sufficiently.

2.3.2 *Non-perturbative decay of the curvaton*

Provided there is no interaction with the thermal bath, the first interaction of the curvaton is non-perturbative production of photons through parametric resonance [10–12]. This is particularly important because of the large photon-curvaton coupling.

EVOLUTION OF THE GAUGE FIELD. We examine the theory for the vector potential A_μ

$$\mathscr{L}_A = (D_\mu\sigma)^\dagger (D^\mu\sigma) - \frac{1}{4e}F^{\mu\nu}F_{\mu\nu} \tag{47}$$

The Euler-Lagrange equations in curved spacetime take the form

$$\partial_\nu \left(\frac{\partial(\sqrt{-g}\mathscr{L})}{\partial(\partial_\nu A_\mu)} \right) - \frac{\partial(\sqrt{-g}\mathscr{L})}{\partial A_\mu} = 0 \tag{48}$$

from which we get the equation of motion for the gauge field $A(t)$

$$\ddot{\mathbf{A}}(t,\mathbf{k}) + H\dot{\mathbf{A}}(t,\mathbf{k}) + \nabla(\nabla\cdot\mathbf{A}(t,\mathbf{k})) - \nabla^2\mathbf{A}(t,\mathbf{k}) + 2e^2(\sigma^\dagger\sigma)\mathbf{A}(t,\mathbf{k}) = 0 \tag{49}$$

by making use of the temporal gauge $A_0 = 0$. In our case, only the transverse component is physical, that is

$$\ddot{A}_k^T(t) + H\dot{A}_k^T(t) + \left(\frac{k^2}{a^2} + 2e^2(\sigma^\dagger\sigma) \right) A_k^T(t) = 0. \tag{50}$$

In order to find the resonance parameters, we need to get rid of the friction term $H\dot{A}_k^T(t)$, which is accomplished by rescaling the field $A_k(t)$ with

$$B_k(t) = a^{1/2}(t)\, A_k(t). \tag{51}$$

Substituting for σ using eq. (45) gives a Mathieu equation with time-dependent parameters,

$$\mathbf{B}''(z,\mathbf{k}) + (\Sigma_k(z) + 2q(z)\,\cos 2z)\;\; \mathbf{B}(z,\mathbf{k}) = 0 \tag{52}$$

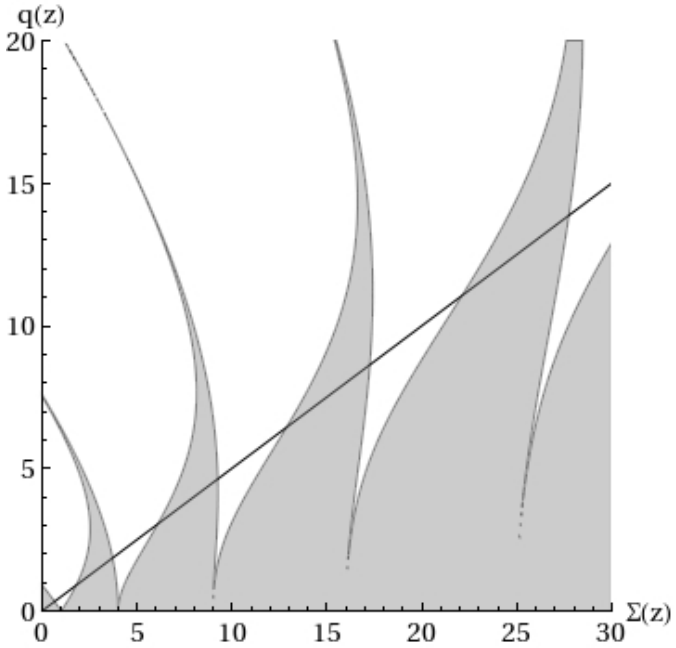

Figure 6: Instability chart of the Mathieu equation. Shaded regions show the stable bands; white regions show resonance bands with exponentially growing solutions. The solid line shows $\Sigma = 2q$. For $k = 0$, the solution moves towards the origin following this line very closely. The starting position and speed at which it moves depend on m and σ_*. Modes with $k > 0$ follow a similar evolution, but along a shallower line. Thus, modes with higher k spend less time in the instability bands, leading to a weaker resonance.

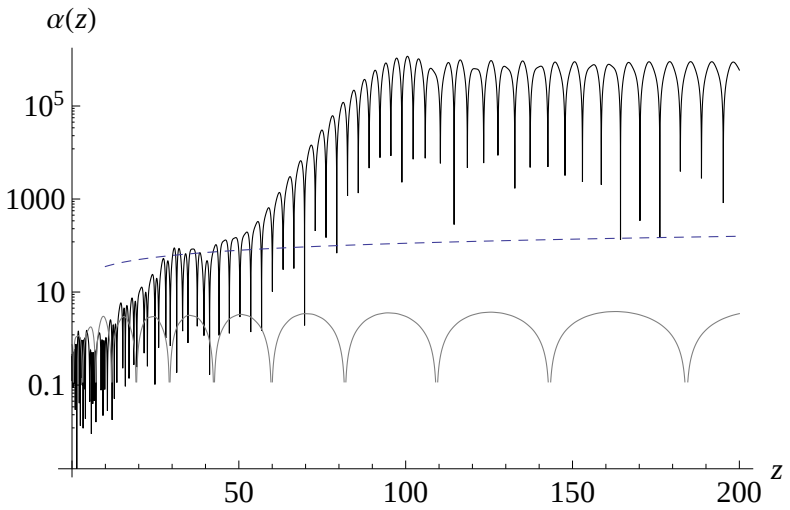

Figure 7: Amplification factor α as a function of z for $k=0$, $\sigma_* = 8H_*$ and $m = 0.1H_*$ (black, upper curve), $m = 0.7H_*$ (grey, lower curve). The dashed line shows the nonlinearity condition (eq. (55)). For $m = 0.1H_*$ a huge amplification is seen and the resonance is clearly nonlinear. For $m = 0.7H_*$, the amplification is much less dramatic and the evolution is expected to remain linear.

where $z = mt$ and coefficients:

$$\begin{aligned} q(z) &\approx \frac{e^2\sigma_*^2}{m^2 z^{3/2}} \\ \Sigma_k(z) &\approx \frac{k^2}{2mH_* z} + \frac{3}{16z^2} + 2q(z). \end{aligned}$$

MATHIEU'S EQUATION. Depending on the parameters Σ and q, the solutions of the Mathieu equation are either oscillatory or exponentially growing. The growing solutions correspond to rapid, resonant energy transfer from the curvaton to the U(1) gauge field. The parameter values for which this happens form instability bands, as shown in fig. 6. In our case, both parameters $q(z)$ and $\Sigma_k(z)$ decrease with time, so that if they are initially large, they move through instability bands, until they leave the last instability band when $q \approx 1$, and the resonance ends. The trajectory for $k=0$ modes is shown in fig. 6. Both the speed at which the solution moves to small values of the parameters, and the initial value depend on m and σ_*. The trajectory for modes with $k>0$ is shallower, and thus modes with large k do not spend enough time in the instability bands to produce a resonance.

In order to estimate the amount of energy transferred from the curvaton fields, we solve eq. (52) numerically, finding the amplification factor $\alpha(z) = A_i(z,\mathbf{k})/A_i(0,\mathbf{k})$.

This is shown in fig. 7 as a function of the time variable z for two sets of parameters. If the amplification factor becomes large, then backreaction can no longer be ignored. We estimate that this happens when

$$\frac{e^2\langle \mathbf{A}^2\rangle}{a(t)^2} \approx m^2. \tag{53}$$

To approximate this, we assume that modes with $k \lesssim k_{\text{res}} \approx \sqrt{em\sigma_*}$ are all amplified by a factor α, and we find

$$\frac{e^2\langle \mathbf{A}^2\rangle}{a(t)^2} \approx \frac{e^2}{8\pi^2}\left(\alpha^2-1\right)\frac{k_{\text{res}}^2}{H_* t}, \tag{54}$$

so that the resonance is non-linear if

$$\alpha(z)^2 \gtrsim 10^3 \frac{z}{\sigma_*/H_*} + 1. \tag{55}$$

In many cases, only a reasonably modest amplification factor α is required in order for the resonance to become non-linear. If the initial value $q_* \approx (e\sigma_*/m)^2/2$ of the resonance parameter q is large, the parameters q and Σ move slowly through a large number of resonance bands. Therefore the amplification factor α becomes exponentially large, and we expect that the dynamics becomes non-linear. In this case a full numerical study is necessary to determine the dynamics. If, on the other hand, $q_* \sim 1$, then the system moves quickly through the resonance bands, and we do not expect significant non-linear effects. fig. 8 shows this initial value of the resonance parameter.

The value of z when the resonance either ends or becomes non-linear is $z_{\text{res}} \lesssim 1000$. It has been shown that for a non-linear resonance, non-relativistic curvaton particles are likely to remain after the resonance has completed [14]. As a very simple estimate we assume that a fraction $f = 0.5$ of the condensate's energy density is transformed to relativistic photons, and half remains as either condensate or non- relativistic curvaton particles. This assumption allows us to use the standard expression (eq. (29)) for the curvature perturbation. However, simulations in a scalar model [14] show that the fraction f is actually highly dependent on the curvaton field value, and this dependence modifies the predicted curvature perturbation significantly. For fully reliable predictions, a non- linear field theory calculation is therefore required.

The fraction of the original curvaton which does not decay resonantly can both interact with the newly-produced thermal bath and decay perturbatively to fermions. The final ζ will include contributions from each process. However, the contribution to the curvature perturbation generated during resonant decay is negligible, $\zeta_{\text{res}} \sim 10^{-14}$, with respect to the observed value of 10^{-5}.

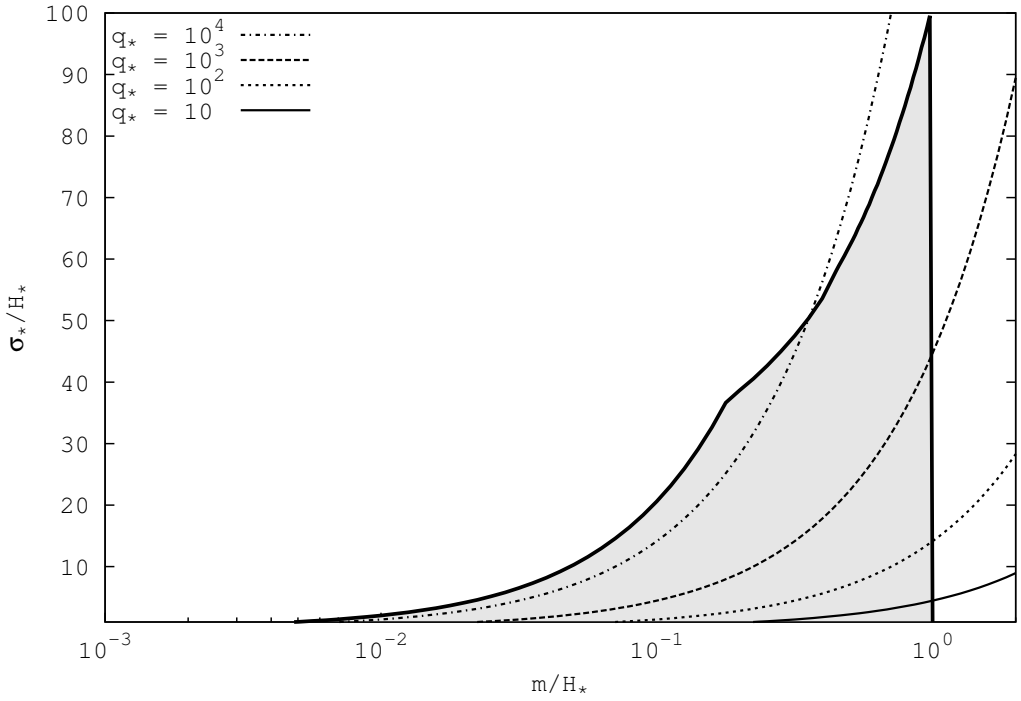

Figure 8: Initial resonance parameter q_* in the allowed parameter space (shaded). The parameter is largest for large σ_*, small m. A stronger, non-linear resonance is expected for larger q_*.

2.3.3 *Subsequent evolution*

After the parametric resonance, we are left with a thermal bath of photons and curvaton condensate leftovers. The resulting picture is similar to the one described in section 2.3.1, where the temperature determines the evolution of the system. The temperature is given by

$$T \simeq 0.4\, \rho_{th}^{1/4} \approx 0.4\, f^{1/4} (m t_{res})^{1/8} \sqrt{\sigma_*/t} \tag{56}$$

and, using eq. (46), the effective rate of thermal interactions is

$$\Gamma_{th}(t \geqslant t_{res}) = 0.011\, e^2\, f^{1/4} (m t_{res})^{1/8} \sqrt{\sigma_*/t}. \tag{57}$$

If $T \ll m$, then the condensate decays into non-relativistic curvaton particles. Because the energy density ρ_σ is still proportional to $1/a^3$, this does not affect the curvature perturbation ζ. Therefore, it is determined by the perturbative decay, which takes place at $t_{pert} \sim 1/\Gamma$, where Γ is the perturbative decay rate. The curvature perturbation ζ is then given by eq. (29), using $r(t_{pert})$.

If $T \gg m$, the thermalized curvatons are ultrarelativistic and the evolution depends on whether chemical equilibrium is reached. This is determined by $t_{chem} = 1/\Gamma_{chem}$, which should be compared to both the timescale of the expansion $(1/H)$ and the time until the relativistic curvaton freezes out again (t_{freeze}). In the case that chemical equilibrium occurs, the curvature perturbation ζ becomes adiabatic, and therefore its final value is determined by the curvaton energy fraction at the time of equilibration r_{th}. This is found to be $\zeta_{th} \sim 10^{-13}$, again far below the observed value of 10^{-5}. Thus, if the curvaton reaches chemical equilibrium with the thermal bath, then the contribution to ζ is negligible.

If, on the other hand, the curvaton does not reach chemical equilibrium, it will eventually become non-relativistic again. The ultra-relativistic period reduces the amplitude of the curvature perturbation ζ. In order to obtain the observed amplitude, the perturbative decay must then be delayed compared with the non- relativistic case. The calculation of ζ follows exactly the same procedure as for the non- relativistic case. The only difference is that a somewhat smaller Γ will be required to obtain sufficient ζ. However, the curvaton must decay before Big Bang Nucleosynthesis (BBN), which means that extremely small values of Γ are not allowed.

2.4 RESULTS

We explore the parameter space numerically, focusing on the observables ζ (curvature perturbation), f_{NL} (non-Gaussianity) and n (CMB spectral index) in turn.

2.4.1 *Curvature perturbation*

In general, the predicted amplitude (eq. (28)) of the curvature perturbation ζ depends on the perturbative decay rate Γ, because it sets the value of t_{dec}. Where possible, we fix Γ in order to obtain $\zeta = 10^{-5}$, however there is a constraint on Γ. The curvaton must decay before BBN, which means that extremely small values of Γ are not allowed. This restricts the low H_*, low m region of parameter space, because [Paper I]

$$r \propto \left(\frac{\sigma_*}{H_*}\right)^2 \left(\frac{H_*}{M_{Pl}}\right)^2 \left(\frac{m}{\Gamma}\right)^{1/2}. \tag{58}$$

Thus low m and low H_* give low r. For $H_* \lesssim 10^8$ GeV the requirement $\zeta = 10^{-5}$ means that there is no available parameter space left. For 10^8 GeV $\lesssim H_* \lesssim 10^9$ GeV, the parameter space is reduced (fig. 9). For $H_* \gtrsim 10^9$ GeV, there is no effect on the parameter space.

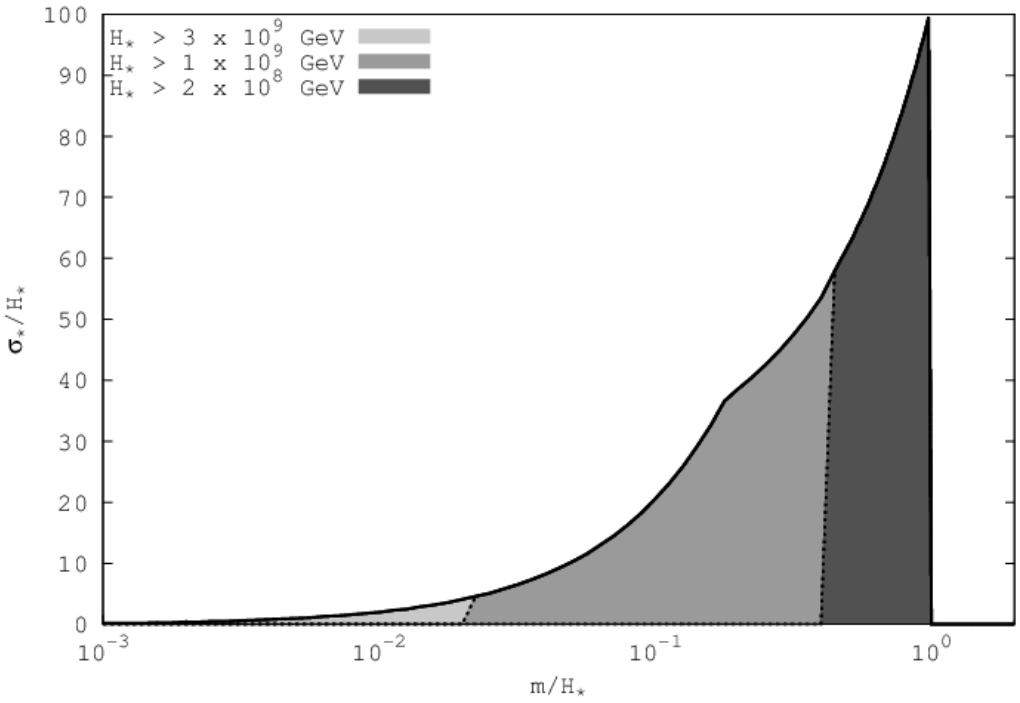

Figure 9: Allowed region for a viable curvaton model which produces $\zeta = 10^{-5}$. For $H_* \gtrsim 3 \times 10^9$, the requirement is satisfied in the entire parameter space (all three shades of grey). The size of the allowed region reduces as H_* reduces. For $H_* = 10^9$ GeV, the allowed region comprises of the two darkest grey regions; for $H_* = 2 \times 10^8$ GeV it is only the dark grey region. For $H_* \lesssim 10^8$ GeV there is no allowed parameter space.

2.4.2 *Non-Gaussianity*

By ignoring the effects of parametric resonance, the value we obtained for $f_{NL} \gtrsim 130$ would rule out the model (Planck [15] restricts f_{NL} of any type to be less than 33). However, because the parametric resonance modifies the predictions significantly, numerical lattice simulations are necessary in order to know the fate of this model.

2.4.3 *Spectral index*

Another observable parameter that could be used to constrain the model is the spectral index n. Unlike ζ and f_{NL}, this depends on the specific model of inflation, and

therefore the results are less generally applicable. Assuming the simple monomial potential

$$V(\phi) = \lambda_\phi \phi^4, \tag{59}$$

the spectral index for the curvature perturbation is

$$\begin{aligned} n &= 1 - 2\epsilon_{\rm inf} + 2\eta_{\rm curv} \\ &\simeq 1 - \frac{2}{N} + \frac{2m^2}{3H_*^2}. \end{aligned} \tag{60}$$

The current observational limits are (Planck + WMAP) $n = 0.9603 \pm 0.0073$ [16]. For $N = 50$ and $N = 60$ e-foldings, n is within the WMAP limits provided $m \lesssim 0.2 H_*$. This would rule out the large m region of the parameter space.

2.4.4 *Cosmic strings*

An additional interesting physical effect could occur because the curvaton field effectively has a non-zero value within any Hubble volume, therefore breaking the Standard Model U(1) symmetry spontaneously. For topological reasons there will be curves in space where the curvaton field vanishes, in very much the same way as in a cosmic string. At the end of inflation, the curvaton fields starts to oscillate, and these strings dissolve, but because the field value is zero at the string locations, they can potentially influence the curvature perturbation on cosmological scales. Furthermore, just like ordinary cosmic strings, these strings carry one quantum of magnetic flux $\Phi_0 = 2\pi/e$, which can also have an effect on the reheating dynamics locally.

3

BARYON-NUMBER VIOLATION AT THE ELECTROWEAK CROSSOVER

Baryon and lepton numbers are classically conserved quantities, but the chiral nature of weak interactions gives rise to the anomalous violation of baryon and lepton number currents at the quantum level. In practice, however, the processes violating B- and L-numbers are suppressed below a temperature scale of $T_c \sim 100\,\mathrm{GeV}$, thus making B and L effectively conserved in the present Universe. Above this critical temperature, which also corresponds to the electroweak scale, sphaleron processes are responsible for baryon number transitions.

3.1 ELECTROWEAK BARYOGENESIS

The idea that baryogenesis might have taken place at the electroweak phase transition was suggested for the first time in 1985 by Kuzmin, Rubakov and Shaposhnikov [17]. However, any successful model of baryogenesis has to fulfill the necessary Sakharov's conditions of B and L non conservation, C and CP violation as well as departure from equilibrium. In the Standard Model, the first requirement is satisfied by the Adler-Bell-Jackiw anomaly, which expresses the fact that, in gauge theories, gauge invariance implies axial vector current non-conservation

$$\partial_\mu J^{\mu 5} = -\frac{e^2}{16\pi^2}\epsilon^{\alpha\beta\mu\nu}F_{\alpha\beta}F_{\mu\nu}, \tag{61}$$

where $J^{\mu 5}$ is the axial vector current, e the gauge coupling, and F_{ij} the gauge field strength tensor. C has been found to be violated in weak interactions [18]. Also CP is violated in the Standard Model in the decays of neutral kaons and in the Cabibbo-Kobayashi-Maskawa matrix. Departure from equilibrium occurs when the rate Γ of

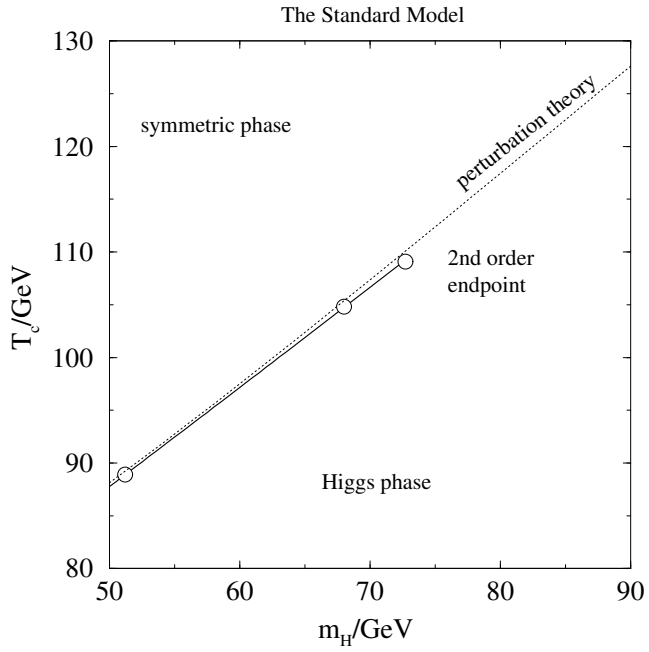

Figure 10: The order of the electroweak phase transition shown in terms of the Higgs mass [22]. The phase transition is first order up to $m_H \sim 70$ GeV, where it becomes second order. For higher values of the Higgs mass, the transition is a crossover.

the process is smaller than the Hubble rate H. In particular, if the electroweak phase transition is first order, bubbles of the new phase nucleate and expand at a substantial fraction of the speed of light [19]. However, Kajantie *et al.* [20] have shown the order of the transition to be dependent on the value of the Higgs mass (figs. 10, 11), being a crossover for $m_H = 125$ GeV. This can be overcome by a minimal modification of the Standard Model that would make the transition first order.

3.2 WEAK INTERACTIONS

The theory of weak interactions is chiral: it couples differently with right- and left-handed fermions. This is evident from the electroweak Lagrangian

$$\begin{aligned}\mathscr{L} \;=\; & i\bar{\psi}_L\gamma^\mu D_\mu\psi_L + i\overline{\psi_R}\gamma^\mu D'_\mu\psi_R - \frac{1}{4}G_{\mu\nu}G^{\mu\nu} - \frac{1}{4}F^a_{\mu\nu}F^{a\mu\nu} \\ & + (D_\mu\phi)^\dagger(D_\mu\phi) + \mu^2\phi^\dagger\phi - \lambda(\phi^\dagger\phi)^2 + \mathscr{L}_Y, \end{aligned} \tag{62}$$

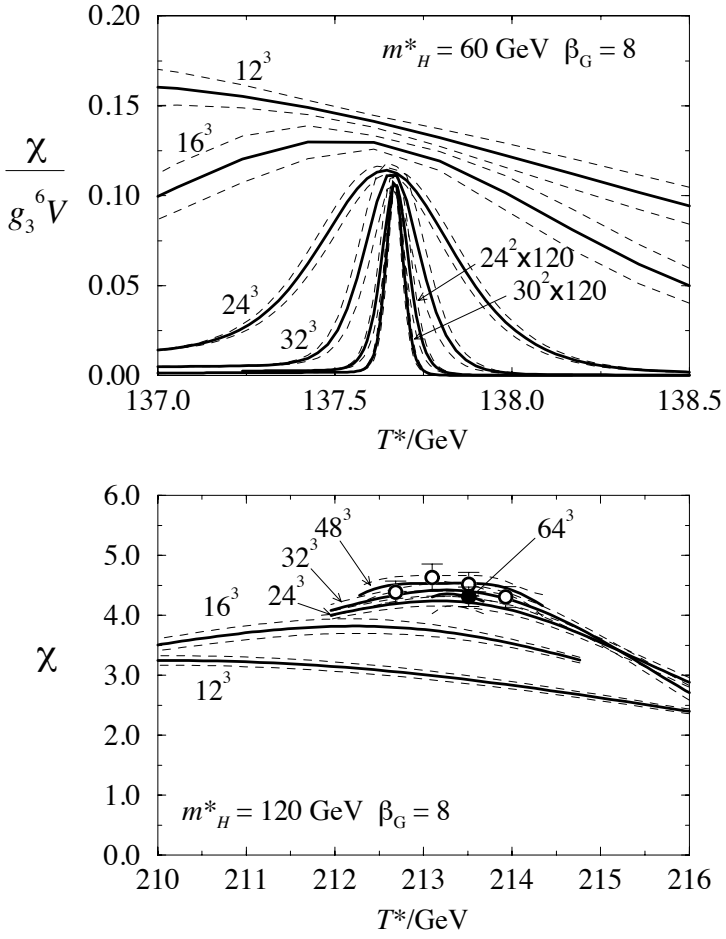

Figure 11: The susceptibility $\chi(T) = g_3^2 V \langle (\phi^\dagger \phi - \langle \phi^\dagger \phi \rangle)^2 \rangle$ of the scalar field ϕ as a function of temperature, at $m_H = 60$ GeV (above) and 120 GeV (below) [20, 21]. Every curve represents a set of simulations with the same lattice volume. In the 60 GeV plot, there is a first-order phase transition, while in the 120 GeV plot, there is a sharp but smooth crossover.

with ψ fermions, $G_{\mu\nu}$ the U(1) field strength, $F^a_{\mu\nu}$ the SU(2) field strength, ϕ the Higgs boson, and $\mathscr{L}_Y$ Yukawa interactions between the fermions and the Higgs field. The covariant derivatives for the SU(2) and U(1) symmetries are, respectively,

$$\begin{aligned} D_\mu &= \partial_\mu + ig\frac{\tau^a}{2} A^a_\mu + ig'\frac{Y}{2} B_\mu \\ D'_\mu &= \partial_\mu + ig'\frac{Y}{2} B_\mu \end{aligned}$$

and the left- and right-handed components of the spinor fields,

$$\psi_L \equiv \frac{1-\gamma_5}{2}\psi \qquad \psi_R \equiv \frac{1+\gamma_5}{2}\psi,$$

include the Dirac matrix γ_5.

Classically, the baryon number current

$$J^\mu_B = \sum_{q=1}^{n_G} \bar{q}\,\gamma^\mu q, \tag{63}$$

with n_G the number of quark generations, is conserved. However, this symmetry need not to be exact as it arises from a global symmetry and not a local one. Indeed, baryon and lepton number conservation is violated at the quantum level, by the Adler-Bell-Jackiw anomaly [23, 24]. The latter is also referred to as the triangle anomaly, as it is produced by triangle graphs of internal fermion loops connected to two vector fields and one axial vector field. Indeed, if we associate the SU(2) or the U(1) gauge bosons at the two vertices of a triangle diagram and a global current corresponding to baryon or lepton numbers at the third vertex, then sum over all the fermions in the standard model will give us non-conserved current

$$\partial_\mu J^\mu_B = \frac{n_G}{64\pi^2}\,\epsilon^{\mu\nu\rho\sigma}\,\left(g^2\,F^a_{\mu\nu}\,F^a_{\rho\sigma} + g'^2\,G_{\mu\nu}\,G_{\rho\sigma}\right) \tag{64}$$

in terms of $F^a_{\mu\nu}$ and $G_{\mu\nu}$, the field strengths for the SU(2) and U(1) gauge fields, respectively,

$$\begin{aligned} F^a_{\mu\nu} &= \partial_\mu A^a_\nu - \partial_\nu A^a_\mu - g\epsilon^{abc} A^b_\mu A^c_\nu \\ G_{\mu\nu} &= \partial_\mu B_\nu - \partial_\nu B_\mu. \end{aligned}$$

The lepton number current is the same as eq. (64). So, given that the number of generations of quarks $n_{G,q}$ and leptons $n_{G,l}$ are the same, $B-L$ is conserved.

3.3 VACUUM STRUCTURE

The theory of anomalies is intimately tied to the physics associated with instantons, which are topologically nontrivial classical solutions of the SU(2) Yang-Mills theory in four dimensions [25]. 't Hooft showed [26] that these solutions give non vanishing contributions to the tunneling amplitudes between nontrivial vacua, leading to baryon and lepton number violation in vector-axial theories. The tunneling cross-section, however, contains an exponential factor of

$$\exp\left(\frac{-16\,\pi^2}{g^2}\right) = \exp\left(-4\pi\,137\,\sin^2\theta_W\right) \approx 10^{-170} \tag{65}$$

which makes this phenomenon practically unobservable.

Each topological vacuum is labeled by a winding number arising from the anomaly. As the U(1) theory does not possess a set of infinite nontrivial vacua unlike the SU(2), we can write the anomaly equation (64) simply as

$$\partial_\mu J^\mu_B = \frac{n_G}{64\pi^2}\,\epsilon^{\mu\nu\rho\sigma}\,g^2\,F^a_{\mu\nu}\,F^a_{\rho\sigma} \;\equiv\; n_G\,\partial_\mu J^\mu_{CS}, \tag{66}$$

from which we obtain the Chern-Simons current J^μ_{CS}

$$J^\mu_{CS} = \frac{g^2}{64\pi^2}\,\epsilon^{\mu\nu\alpha\beta}\,\mathrm{Tr}\left(A_\nu F_{\alpha\beta} + i\frac{g}{3}\,A_\nu A_\alpha A_\beta\right). \tag{67}$$

The integral of the non-Abelian chiral anomaly is an integer, the Chern-Simons number

$$N_{CS} = \int d^3x\, j^0_{CS} = -\frac{g^2}{64\pi}\int d^3x\,\epsilon^{ijk}\mathrm{Tr}\left(A_i F_{jk} + i\frac{g}{3}A_i A_j A_k\right), \tag{68}$$

representing the topological winding numbers corresponding to the infinite set of "pure gauge" degenerate vacua of the electroweak sector of the Standard Model. The question of baryon and lepton number violation in the Standard Model therefore becomes a question of whether dynamics allow transitions from one vacuum to another.

At zero temperature transitions occur via instantons [27], and the rate is negligible even on cosmological scales, see eq. (65). The Standard Model Higgs field acquires a vacuum expectation value $\langle|\phi|\rangle = v/\sqrt{2}$, with $v = 246\,\mathrm{GeV}$.

However, at finite temperatures $T > 100\,\mathrm{GeV}$, thermal fluctuations can lead to spontaneous transitions by surmounting the potential barrier with a diffusion rate (the so-called sphaleron rate) of

$$\Gamma_{sphaleron}(T) = \lim_{V,t\to\infty}\frac{\langle[N_{CS}(t) - N_{CS}(0)]^2\rangle}{Vt}. \tag{69}$$

Each transition from one vacuum to the adjacent one produces [17, 28]

$$n_G\cdot[N_{CS}(t) - N_{CS}(0)] \;=\; B(t) - B(0) \;=\; L_i(t) - L_i(0), \tag{70}$$

thus a change in the Chern-Simons number by one unit creates three baryons and three leptons. The Higgs vev is $\langle|\phi|\rangle \approx 0$, and there is a "symmetry breaking" transition between the symmetric and broken phases.

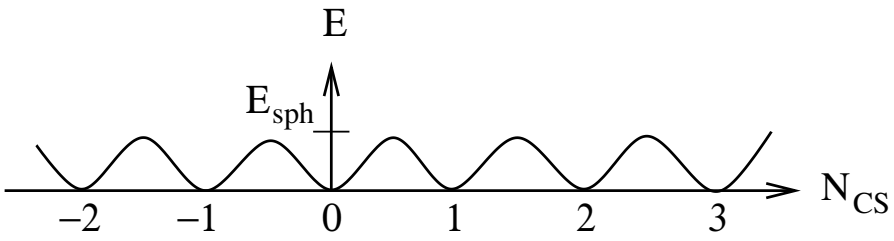

Figure 12: Vacuum structure of the pure-gauge electroweak theory. The energy of gauge field configurations is displayed as a function of Chern-Simons number [30]. For the theory with baryons, see fig. 13.

3.4 SPHALERON RATE AND BARYOGENESIS

At high temperatures the transitions can occur because the temperature is high enough to allow for thermal fluctuations [17]. The sphaleron rate can be estimated in the broken-phase regime as

$$\Gamma_{\mathrm{sphaleron}} = \kappa \cdot \exp\left(\frac{-\Delta F}{T}\right), \tag{71}$$

where κ is a prefactor and the rest is the Boltzmann factor, with F as the free energy.

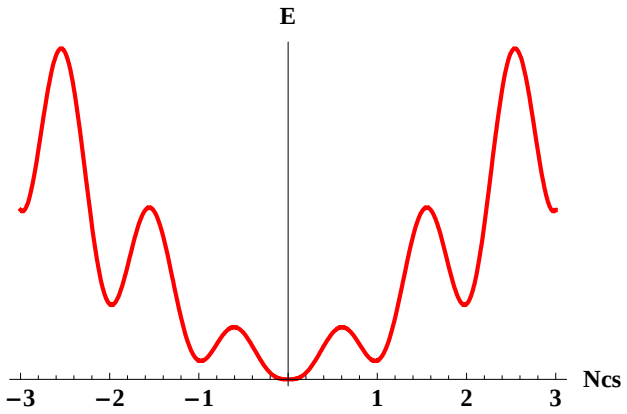

Figure 13: Vacuum structure of the electroweak theory in the presence of baryons. When you add baryons, the energy E (as a function of Chern-Simons number N_{CS}) becomes very slightly parabolic, with a minimum at 0, reflecting the cost of having too many baryons. Therefore, at high temperatures, B averages to zero in the absence of chemical potential. Here the parabolic shape is exaggerated.

Klinkhamer and Manton [32] found an approximation for the free energy of the sphaleron

$$F_{sphaleron} = \frac{4\pi v}{g} F_0\left(\lambda/g^2\right) \tag{72}$$

where the factor F_0 ranges between 1.566 and 2.722 and v is the vacuum expectation value, with a characteristic energy of $4\pi v/g \approx 5$ TeV. The size of the sphaleron is $1/gv$. The Chern-Simons number of the sphaleron is half integer, that is, the sphaleron is in the middle of two vacua with integer-valued baryon numbers.

The change in free energy ΔF, occurring when moving between two non- equivalent baryon number configurations, is also determined by the baryon chemical potential μ_B and particle number N_B, which result in an extra factor of

$$\frac{\Delta N_B \mu_B + \Delta N_L \mu_L}{T}. \tag{73}$$

By imposing equal baryon- and lepton-number densities and [33]

$$\Delta N_B = \Delta N_L = \pm n_G/2,$$

we get the relation between the sphaleron rate and the rate of baryon number violation

$$\frac{dN_B}{dt} = -n_G^2 \frac{3}{2} \frac{\mu_B}{T} \Gamma_{sph}, \tag{74}$$

which yields

$$\frac{1}{N_B}\frac{dN_B}{dt} = -\kappa\left(\lambda/g^2\right) 1100\, g^7 v \exp\left[\frac{4\pi v}{g} F_0\left(\lambda/g^2\right)\right] \tag{75}$$

where κ is a factor, which needs to be calculated numerically [34–36]. The temperature range where this formula is valid is $T = 16 - 480$ GeV, the electroweak energy scale.

3.5 NON-PERTURBATIVE METHODS

The temperatures at which baryon number violation takes place through sphaleron processes cannot be observed in nature, nor reproduced in experiments such as the LHC. Moreover, perturbative methods for the sphaleron decay remain well defined in the broken phase, but, at temperatures near the electroweak transition, infrared divergences occur and cannot be tamed. The electroweak theory is addressed with perturbative methods down to the modes with momenta $k \leqslant g^2 T$, which are non-perturbative, and we need to make use of lattice techniques [37].

In our study, we used two plausible values for the Higgs mass, 115 GeV and 160 GeV (Paper II). Along with the discovery of the Higgs boson at CERN in 2012, we complemented our previous work for the found Higgs mass of $m_H = 125$ GeV (Paper III).

3.5.1 *Dimensional reduction*

The full four-dimensional Standard Model with chirally coupled fermions is too cumbersome to simulate on the lattice. However, for static thermodynamics we can use the fact that the weak coupling constant is small, and apply perturbation theory only to modes which can be reliably treated with perturbative methods: that is, to modes with momentum $k > g^2T$. This procedure is called dimensional reduction, because it results in a three-dimensional effective theory for the soft (g^2T) modes. The effective theory is purely bosonic, and it fully includes the essential non-perturbative physics. The detailed description how this is performed can be found in ref. [31, 38, 39]; for earlier and related work, see [40–45].

The perturbative derivation of the effective theory is based on the hierarchy between the hard ($k \gtrsim \pi T$), electric ($k \sim gT$) and magnetic ($k \sim g^2T/\pi$) scales of a Euclidean finite-temperature path integral. In the first stage we integrate over the hard scales, obtaining an effective theory of scales $k \lesssim gT$. Because of the definition of the Matsubara frequencies as in eq. (114), all fermionic modes and non-static ($k_0 \neq 0$) bosonic modes are of order πT. Thus, the effective theory is purely bosonic and three dimensional. Concretely, the actual "integration" is done by writing down a general renormalizable effective theory and matching the perturbatively- computed two-, three- and four-point functions in both the effective theory and in the original four-dimensional theory, thus fixing the parameters of the effective theory.

The effective theory can be further simplified by integrating over scales gT, which gives us the three-dimensional SU(2) gauge theory coupled to the Higgs field.

The three-dimensional, effective Lagrangian reads

$$\mathscr{L}_{\text{eff}} = \frac{1}{4} F_{ij}^a F_{ij}^a + (D_i\phi)^\dagger (D_i\phi) + m_3^2 \phi^\dagger \phi + \lambda_3 (\phi^\dagger \phi)^2, \tag{76}$$

with parameters

$$\begin{aligned} m_3^2 &= \left(\frac{3}{16} g^2 + \frac{1}{2}\lambda\right) T^2 - \mu^2 \\ g_3^2 &= g^2 T \\ \lambda_3 &= \lambda T, \end{aligned} \tag{77}$$

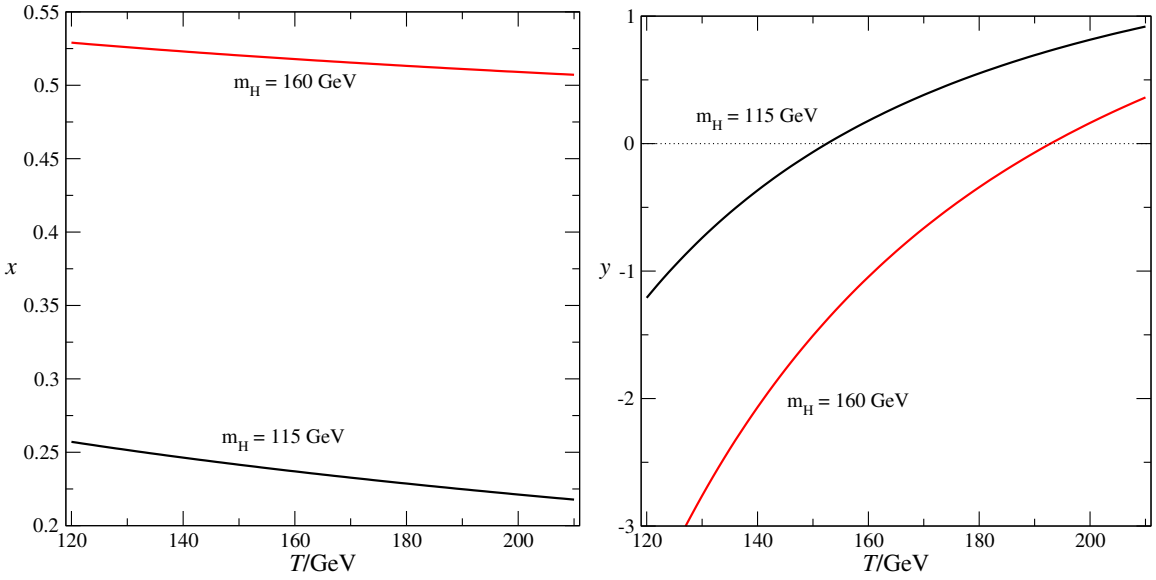

Figure 14: The values of x (left) and y (right) for $m_H = 115$ and 160 GeV in the temperature range of the electroweak crossover. Figure taken from Paper II.

which depend on temperature and the parameters of the Standard Model; the full expressions are given in ref. [31]. The U(1) field is omitted because its effect on the transition is numerically small [20].

The coupling constants of the theory are g_3^2, m_3^2 and λ_3 of eq. (77), however it is customary to use dimensionless quantities x and y and express the set of the parameters of the effective theory as

$$g_3^2, \qquad x = \frac{\lambda_3}{g_3^2}, \qquad y = \frac{m_3^2}{g_3^4}. \tag{78}$$

Here the dimensionful parameter g_3^2 sets the scale and the physics is completely determined by the values of x and y. The values of x and y depend on the Higgs mass; in fig. 14 their values are shown for $m_H = 115$ GeV and $m_H = 160$ GeV. The other significant Standard Model parameters which influence the values of x and y are:

G_F	=	1.16639×10^{-5}	Fermi coupling
m_Z	=	91.1876 GeV	Z boson mass
m_W	=	80.425 GeV	W boson mass
m_t	=	174.3 GeV	top mass
$\alpha(m_W)$	=	0.1187	strong coupling constant.

Now we can express the Boltzmann factor for a sphaleron configuration of eq. (71) in terms of the SU(2) gauge field and Higgs field in the broken phase [17] as

$$\exp\left(\frac{-F_{\text{sphaleron}}}{T}\right) = \exp\left(-\int_0^\beta d\tau \int d^3x\, \mathscr{L}_{\text{eff}}\left(A_i^a(x), \phi(x)\right)\right), \tag{79}$$

with effective Lagrangian given by eq. (76).

3.5.2 *Lattice-continuum relations*

After building the continuum 3D theory from the 4D fundamental one, we have to put it on the lattice. The common lattice discretization of the action is [46]

$$\begin{aligned} S_{\text{Lat}} &= \beta_G \sum_x \sum_{ij}\left(1-\frac{1}{2}\text{Tr}\left[P_{ij}\right]\right) - \beta_H \sum_x \sum_i \frac{1}{2}\text{Tr}\left[\phi^\dagger(x) U_i(x)\phi(x+\hat{i})\right] + \\ &+ \sum_x \frac{1}{2}\text{Tr}\left[\phi^\dagger(x)\phi(x)\right] + \beta_R \sum_x \left[\frac{1}{2}\text{Tr}\left[\phi^\dagger(x)\phi(x)\right]-1\right]^2, \end{aligned} \tag{80}$$

which is constructed only with gauge-invariant terms. Here $U_i(x)$ is the SU(2) gauge link variable, P_{ij} is the standard ij-plane plaquette constructed from the link variables, and the lattice Higgs field is naively scaled from the continuum field with

$$\frac{1}{8}\beta_G\beta_H(\phi^\dagger\phi)_{\text{lat}} = \frac{(\phi^\dagger\phi)_{\text{cont}}}{g_3^2}.$$

The parameters β_G, β_H and β_R are related to the parameters $g_3^2 a$, x and y by

$$\beta_G = \frac{4}{g_3^2 a}, \tag{81}$$

$$x = \frac{1}{4}\lambda_3 a \beta_G = \frac{\beta_R \beta_G}{\beta_H^2}, \tag{82}$$

$$\begin{aligned} y &= \frac{\beta_G^2}{8}\left(\frac{1}{\beta_H} - 3 - \frac{2x\beta_H}{\beta_G}\right) + \frac{3\Sigma\beta_G}{32\pi}(1+4x) + \frac{1}{16\pi^2} \\ &\quad \times\left[\left(\frac{51}{16}+9x-12x^2\right)\left(\ln\frac{3\beta_G}{2}+\zeta\right)+5.0+5.2x\right]. \end{aligned} \tag{83}$$

Here $\Sigma = 3.1759115$ and $\zeta = 0.08849$ and the other numerical constants appearing in eq. (83) are specific for the SU(2) + Higgs model and are computed in [47].

The continuum limit is taken using equations (81)–(83) by letting $\beta_G \to \infty$ while keeping x, y and g_3^2 constant. The counterterms in eq. (83) remove the linear and logarithmic divergences in the lattice spacing a.

The gauge invariant Higgs field expectation value $\langle\phi^\dagger\phi\rangle$ has linear and logarithmic UV divergences. Subtracting the divergences from the lattice expectation value, we obtain the continuum quantity $\langle\phi^\dagger\phi\rangle$ as [46] using

$$\begin{aligned}\frac{\langle\phi^\dagger\phi\rangle_{\rm cont}}{g_3^2} &= \frac{1}{8}\beta_G\beta_H\left(\langle\phi^\dagger\phi\rangle_{\rm lat}-\frac{\Sigma}{\pi\beta_H}\right)-\frac{3}{(4\pi)^2}\left(\log\frac{3\beta_G g_3^2}{2g_3^2}+\zeta+\frac{1}{4}\Sigma^2-\delta\right)\\ &+ \mathcal{O}\left(\frac{1}{\beta_G}\right),\end{aligned} \tag{84}$$

where $\zeta+\frac{1}{4}\Sigma^2-\delta\approx 0.6678$.

3.5.3 *Real-time evolution*

The effective theory in eq. (76) is well understood and has been very successfully used in studies of static thermodynamical quantities of hot electroweak physics. As such, it does not describe dynamical phenomena, which include sphaleron transitions. It is possible to take the theory in eq. (76) and use the classical equations of motion to describe the time evolution of the fields, as was done in the early studies of the sphaleron rate [48–50]. However, it has been shown that the classical theory contains divergent UV contributions to the gauge field dynamics, and the results are cut-off dependent [51, 52]. Hence, technically the infrared gauge field dynamics of the classical theory do not exist. The physical origin of the problem is that the Landau damping of the transverse gauge fields in the classical theory is UV divergent, and the theory does not have a physical continuum limit.

These problems can be improved by studying classical theory with hard thermal loop (HTL) effects included [53]. This leads to complicated and expensive numerical implementations [54, 55]. However, as first demonstrated by Bödeker [56], the physical damping makes the dynamics of the infrared gauge field modes (modes with $k\lesssim g^2T$) to be fully overdamped. Then, at leading order in $1/\ln(1/g)$ the evolution of these modes is described with simple Langevin dynamics (in $A_0=0$ gauge, and identifying $H/T=S$, the action of eq. (76)) [57]:

$$\partial_t A_i = -\sigma_{\rm el}^{-1}\frac{\partial H}{\partial A_i}+\xi_i^a, \tag{85}$$

where $\sigma_{\rm el}$ is the non-Abelian "color" conductivity,

$$\sigma_{\rm el}^{-1} = \frac{3\gamma}{m_D^2}, \tag{86}$$

$$\gamma = \frac{2g^2T}{4\pi}\left(\ln\frac{m_D}{\gamma}+3.041\right), \tag{87}$$

and the Debye mass $m_D^2 = (11/6)g^2T^2$ in the Standard Model. ξ is a random Gaussian noise with

$$\langle \xi_i^a(\mathbf{x},t)\xi_j^b(\mathbf{x}',t')\rangle = 2\sigma_{el}T\delta_{ij}\delta^{ab}\delta(\mathbf{x}-\mathbf{x}')\delta(t-t'). \tag{88}$$

The Higgs field has parametrically much less damping. Hence, it can also be evolved with a Langevin equation, but with a much faster rate of evolution. To this accuracy we can take it to be infinitely fast in comparison with the gauge field evolution [29]. Iterating eq. (87), we can solve for $\gamma = 0.66361688\ g^2T$.

In principle the Langevin evolution is straightforward to implement on the lattice. However, it is unnecessarily slow: we can substitute it with any dissipative update, as long as the relation between the evolution rates is known. Thus, it is much more efficient to use random-order heat-bath update algorithm for the SU(2) gauge fields [58, 59]. At leading order in small a, n full heat-bath update sweeps through the lattice correspond to the real-time step [59]

$$\Delta t = \frac{1}{4}\sigma_{el}\, a^2 n\,. \tag{89}$$

The Higgs field is updated with a mixture of heat bath and overrelaxation much more frequently than the gauge field [59].

3.6 MEASURING THE SPHALERON RATE

The evolution of the Chern-Simons number N_{CS} over a time interval (t_0, t) can be defined using lattice electric and magnetic fields:

$$\delta N_{CS}(t) \equiv N_{CS}(t) - N_{CS}(t_0) = \frac{g^2}{8\pi^2}\int_{t_0}^{t} dt' \int d^3x E_i^a B_i^a. \tag{90}$$

Unfortunately the topology on the lattice is not well defined, and using naive lattice scale E and B fields the right-hand side of eq. (90) contains ultraviolet noise. This gives unphysical diffusion not connected with the sphaleron rate. The method of *calibrated cooling* [48, 50], offers a way out of the problem. It is based on the fact that at small enough lattice spacing sphalerons are large in lattice units, with a dominant length scale of order $1/(g^2T)$. By applying a pre-determined amount of cooling (Langevin evolution without the noise) to the lattice gauge fields, the ultraviolet noise is eliminated, without compromising the long-distance topology of the configuration. At this point it is possible to evaluate the integral in eq. (90) with only small errors. Cumulative residual errors are eliminated by periodically cooling all the way down to a vacuum configuration and correcting for deviation from integer values of δN_{CS} between two vacua. This is schematically described in fig. 15. By adjusting the cooling

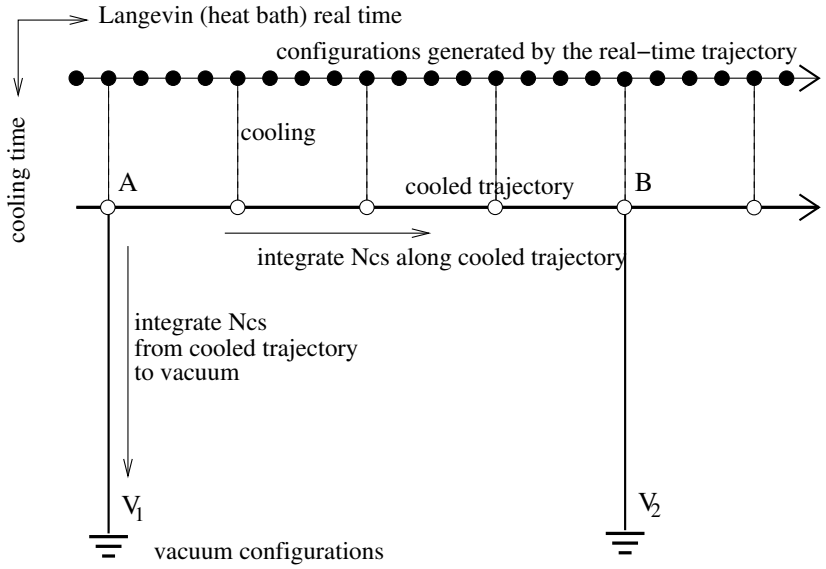

Figure 15: Measurement of the Chern-Simons number evolution [50]. The solid circles show the configurations generated by the real-time evolution using the Langevin/heat-bath method. At fixed intervals, the configurations are cooled by the same amount in order to construct a cooled trajectory, where the UV noise is almost completely eliminated, allowing to calculate δN_{CS} from eq. (90). The cooling from vacuum to vacuum works as a test for residual errors: δN_{CS} must then be close to an integer, the deviations from which are subtracted, thus avoiding the accumulation of errors.

parameters so that these deviations from integers always remain much smaller than unity, we also ensure that the cooling is sufficient to keep the measurement topological.

Cooling the original gauge fields close to the vacuum is computationally very expensive. The procedure is dramatically accelerated by "blocking", that is reducing the lattice gauge fields by a factor of two after the UV noise has been sufficiently eliminated; this is repeated a couple of times until a minimum lattice size (6 in our case) has been reached. The remainder of the cooling then proceeds 2^5 times faster, 2^3 because the lattice is smaller and 2^2 because we can use a Δt step size which is larger in physical units [50].

3.6.1 *Sphaleron rate in the symmetric phase*

We calculated the sphaleron rate using two different, and complementary, methods. We started at high temperatures, above the cross-over, and went through the whole

crossover range into the "broken phase" by uniformly decreasing the temperature. At high temperatures we use standard canonical Monte Carlo sampling. As the potential barrier between consecutive Chern-Simons numbers is low, the probability distribution over Chern-Simons number is approximately flat. As the temperature is decreased, the sphaleron rate becomes exponentially suppressed and the canonical real-time method is too inefficient to resolve the slow rate. At this point we began using multicanonical simulations.

As an example, the evolution of the Chern-Simons number at $m_H = 115\,\mathrm{GeV}$ and with $T = 152\,\mathrm{GeV}$ (symmetric phase), 145 GeV (cross-over region) and 140 GeV (broken phase) is shown in fig. 16. In the symmetric phase the transitions are unsuppressed and it is straightforward to measure the diffusion rate. Around the cross-over temperature the probability distribution of ΔN_{CS} becomes peaked around integer values and the transitions between these values become rapidly more suppressed. Finally, deep in the broken phase the rate goes down until we are not able to measure it with the real-time evolution method.

3.6.2 *Sphaleron rate in the broken phase: multicanonical method*

At low temperatures where the sphaleron rate is strongly suppressed, this can be measured using a multicanonical method similar to the one used in [50]. The calculation consists of two stages:

i) the measurement of the potential barrier (probabilistic suppression) between two integer vacua,
ii) the calculation of the rate of the tunneling through the top of the potential barrier.

The measurement of the potential barrier is the multicanonical stage of the computation. As is usually done in a multicanonical context, instead of sampling configurations with the canonical weight

$$P_{can}(U,\phi) \propto e^{-S(U,\phi)}, \tag{91}$$

we compensate for the strong suppression by adding a carefully-chosen weight function $W(N_{CS})$, which is a function of the order parameter, in this case the Chern-Simons number. The configurations $\{U,\phi\}$ are now sampled with the probability density

$$P_{muca}(U,\phi) \propto e^{-S(U,\phi)+W(N_{CS}[U])}. \tag{92}$$

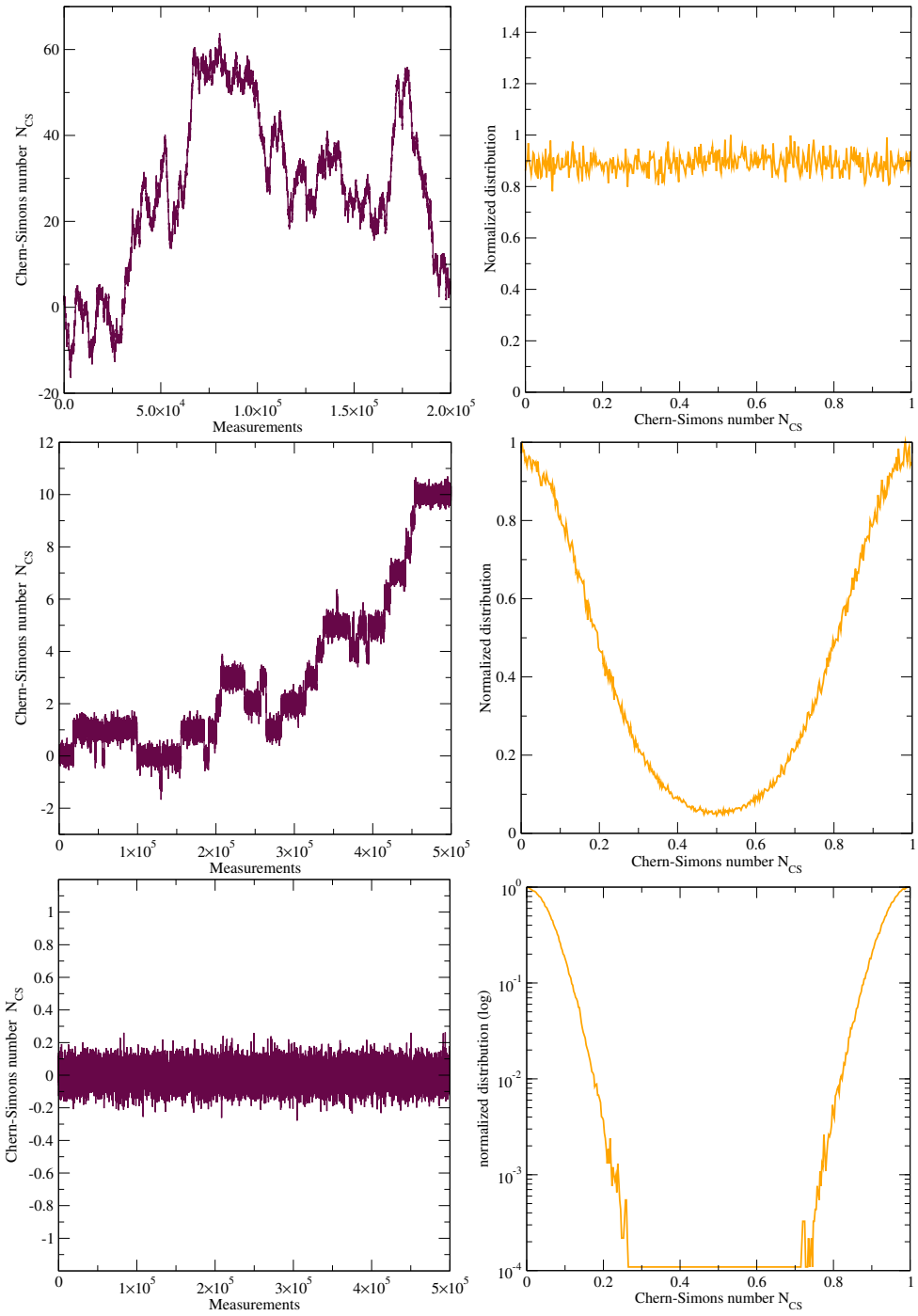

Figure 16: N_{CS} from a heat-bath trajectory (left), and the resulting probability distribution (right), folded into the interval $[0,1]$, at $m_H = 115\,\mathrm{GeV}$ and $T = 152$ (top), 145 (middle) and 140 GeV (bottom). At high temperature, in the symmetric phase, the sphaleron transitions are unsuppressed, whereas at low T the transitions are so strongly suppressed that they do not occur in canonical simulations.

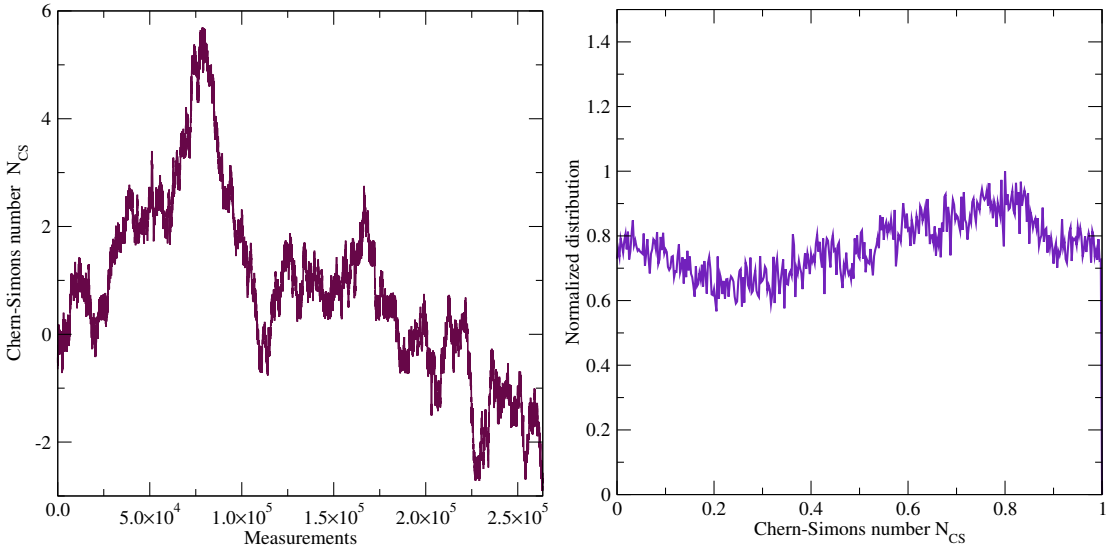

Figure 17: A heat-bath trajectory for N_{CS}, again for $m_H = 115\,\mathrm{GeV}$ and $T = 140$ but now with multicanonical simulations (left), and the corresponding multicanonical probability distribution P_{muca} (right).

Defining the physical (canonical) probability distribution of the Chern-Simons number

$$p_{can}(N'_{CS}) = \int dU\, d\phi\, P_{can}[U,\phi]\, \delta(N'_{CS} - N_{CS}[U]), \tag{93}$$

it is clear that the corresponding multicanonical distribution is

$$p_{muca}(N_{CS}) = p_{can}(N_{CS})\, e^{W(N_{CS})}. \tag{94}$$

Thus, the probability suppression in multicanonical simulations vanishes if we choose $W(N) = -\ln p_{can}(N) + \mathrm{const}$. This is not a particularly useful result because we do not know the canonical distribution a priori; indeed, that is the quantity we set out to compute with the multicanonical method.

However, it is possible to calculate a good enough approximation for W by using an automatic iterative "self-learning" procedure, as in [59]. Essentially, during the learning stage the weight function is continuously modified in order to maximize the flatness of the total distribution of the Chern-Simons number. When the iteration has sufficiently converged, the resulting weight function W is then used in a production run.

The physical (canonical) Chern-Simons probability distribution is now obtained from the measured multicanonical distribution using eq. (94). An example of the multicanonical evolution and the resulting probability distribution is shown in fig. 17,

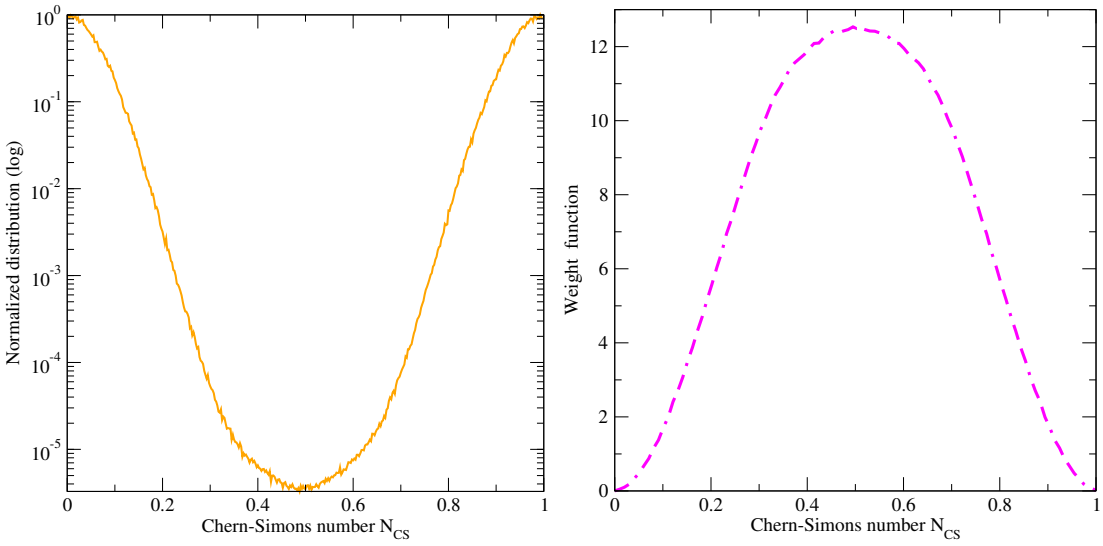

Figure 18: The physical distribution P_{can} (left), after reweighting the result in fig. 17 with the multicanonical weight function (right).

for $m_H = 115\,\mathrm{GeV}$ and $T = 140\,\mathrm{GeV}$; the same parameters as the lowest temperature in fig. 16. Here the "evolution" cannot be interpreted as a physical evolution in real time. As we can observe, the distribution of the Chern-Simons number is now almost flat. The resulting canonical (physical) probability distribution is shown in fig. 18, together with the weight function $W(N_{CS})$ used.

We obtain an estimate for the physical expectation value for a general observable A from multicanonical simulation from

$$\langle A \rangle = \frac{\sum_i A_i e^{-W_i}}{\sum_i e^{-W_i}}, \tag{95}$$

where the sums go over the configurations $\{U,\phi\}_i$ obtained from the simulation and on which the measurements are performed, $W_i = W(N_{CS}[\{U\}_i])$ and $A_i = A(\{U,\phi\}_i)$.

The multicanonical probabilistic weight is implemented as an accept/reject step as follows:

i) start with configuration A, with weight function W_A;
ii) perform one heat-bath sweep through the lattice, producing provisional new configuration B;
iii) measure $N_{CS}(B)$ as described above, obtaining W_B.
iv) the new configuration is accepted with probability

$$p_{\mathrm{accept}}(A \to B) = \begin{cases} 1 & \text{if } W_A \leqslant W_B \\ e^{W_B - W_A} & \text{if } W_A > W_B. \end{cases} \tag{96}$$

If the update is rejected, we start again at point i) with configuration A. The acceptance rate was around 50% at the lowest temperatures used, and increased at higher temperatures.

Obviously, the measured value of N_{CS} depends on the amount of cooling applied before the measurement. Thus, the obtained probability distribution $p(N_{CS})$ is also cooling dependent. However, this is completely cancelled by the dynamical rate measurement described in section 3.6.3, so that the final rate is independent of the amount of cooling. Nevertheless, the right amount of cooling must be judiciously chosen for efficiency: insufficient cooling gives too noisy observables, whereas too much cooling takes one too far "downhill" from the original configuration towards the vacuum.

3.6.3 *Sphaleron rate in the broken phase: dynamical prefactor*

The multicanonical procedure described above gave us the probability distribution of the Chern-Simons number in the broken phase. We can now measure the tunneling rate following refs. [50, 59]:

1. Let us assume that we have carried out the multicanonical simulations and obtained the canonical (physical) probability distribution of the Chern-Simons number $p_{\rm phys}(N_{CS})$.

2. We choose a narrow interval $1/2-\epsilon/2 \leqslant N_{CS} \leqslant 1/2+\epsilon/2$ around the point that separates the vacuum $N_{CS}=0$ from the vacuum $N_{CS}=1$. The relative probability of finding a configuration here is

$$P(|N_{CS}-1/2| \ \epsilon/2) = \int_{1/2-\epsilon/2}^{1/2+\epsilon/2} dN \, p_{\rm phys}(N). \tag{97}$$

   This is where we need multicanonical methods, as the probability of being on top of the barrier is extremely small, and to get a reliable estimate would take an impractically long time with canonical sampling.

3. Let us now take a random configuration from the canonical distribution but with the constraint $1/2-\epsilon/2 \leqslant N_{CS} \leqslant 1/2+\epsilon/2$; i.e. near the top of the potential barrier. Starting from this configuration, we now generate two real-time trajectories using the heat-bath dynamics, as described in section 3.6.1. The trajectories are evolved until the Chern-Simons number falls near a vacuum value. Interpreting one of the trajectories as evolving backwards in time, we can glue the trajectories together at the starting point and obtain a vacuum-to-vacuum trajectory. The trajectory can either return to the starting vacuum or

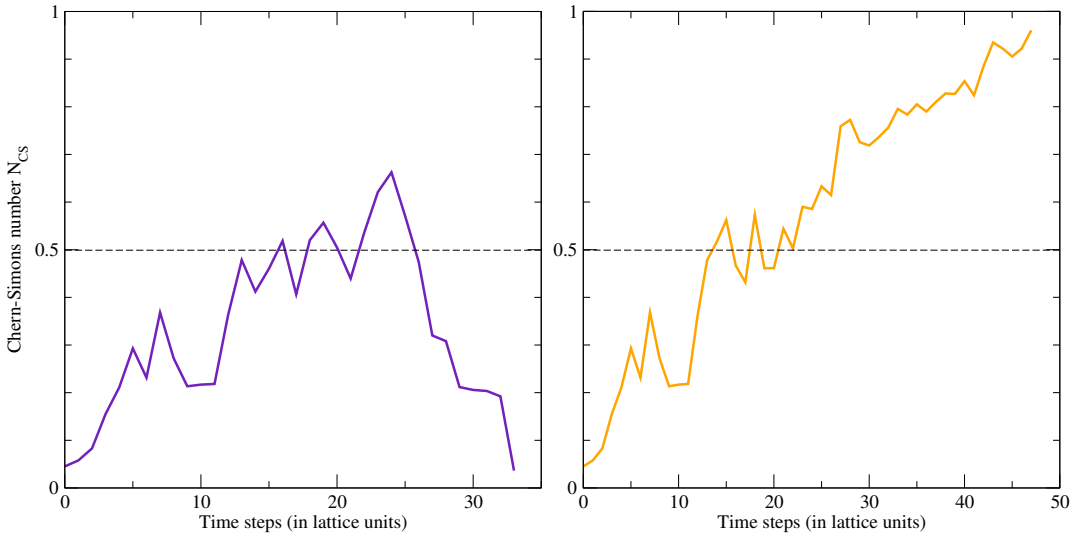

Figure 19: Two real-time trajectories starting from the same configuration. The final and initial configuration can either be the same (left) or different (right). The trajectories cross the central value of our order parameter $N_{CS} = 1/2$ several times, a fact we compensate for through the dynamical prefactor eq. (98).

be a genuine tunneling trajectory, see fig. 19. Only the latter-type trajectories contribute to the sphaleron rate.

4. We can obtain the tunneling rate by measuring $|\Delta N_{CS}/\Delta t|$ from the trajectories at the moment they cross the value $N_{CS} = 1/2$. Here Δt is the time interval between successive measurements, and ΔN_{CS} the change in Chern-Simons number. This characterizes the probability flux thorough the top of the barrier. We obtain the physical time difference from the relation between the heat-bath "time" and physical time, eq. (89).

5. If the tunneling trajectories would go straight across the top, the ingredients above would be sufficient to calculate the total rate. However, typically the trajectories "random walk" near the top of the barrier and can cross the value $N_{CS} = 1/2$ several times. Because the trajectories were chosen starting from a set of configurations near the top of the barrier, this leads to overcounting: the evolution could be started at any point the $N_{CS} = 1/2$ limit is crossed. This can be compensated by calculating a dynamical prefactor

$$d = \frac{1}{N_{\text{traj}}} \sum_{\text{traj}} \frac{\delta_{\text{tunnel}}}{\#\text{ crossings}}, \tag{98}$$

where the sum goes over the ensemble of trajectories, $N_{\rm traj}$ is the number of trajectories, $\delta_{\rm tunnel}$ is 0 if the trajectory does not lead to a change of the vacuum and 1 if it does, and (# crossings) is the number of times the trajectory crosses $N_{\rm CS} = 1/2$.

With these ingredients, the sphaleron rate now becomes

$$\Gamma = \frac{P(|N_{\rm CS} - 1/2| \ \epsilon/2)}{\epsilon} \langle |\frac{\Delta N_{\rm CS}}{\Delta t}| \rangle \, {\rm d}. \tag{99}$$

We note that the result is independent of ϵ as long as $\epsilon \ll 1$. It is also independent of the frequency Δt with which the Chern-Simons number is measured. Equation (99) has a well-defined continuum limit [Paper II].

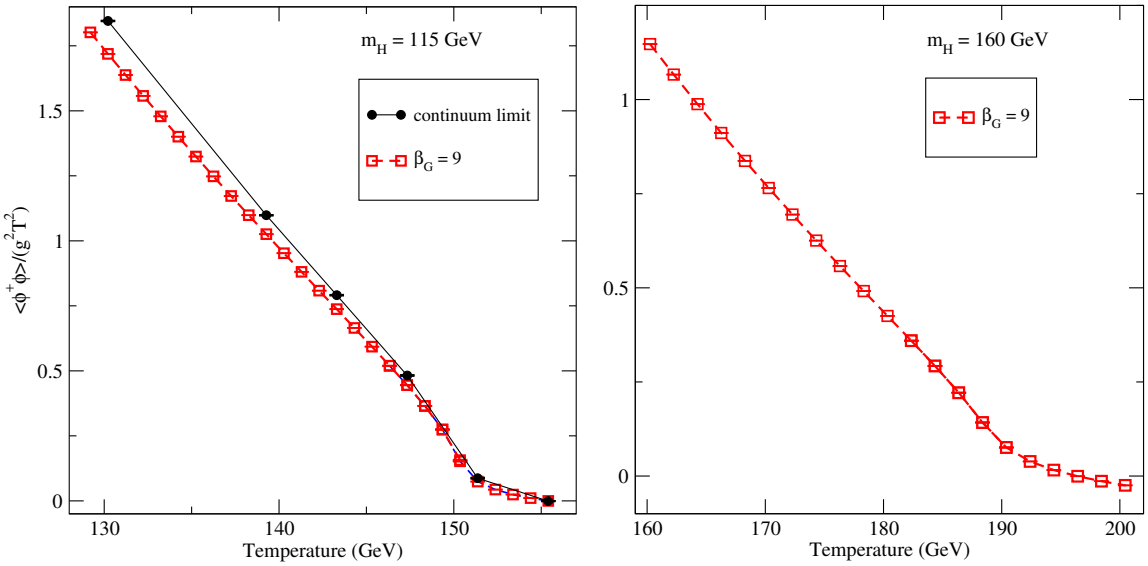

Figure 20: The Higgs field expectation value for $m_{\rm H} = 115\,{\rm GeV}$ (left) and 160 GeV (right). Squares are for $\beta_{\rm G} = 9$, volume $(L/a)^3 = 32^3$. For $m_{\rm H} = 115\,{\rm GeV}$ we have performed the continuum limit extrapolation at selected temperatures using a range of lattice spacings $\beta_{\rm G} = 4/(g_3^2 a) = 6 \ldots 12$ and extrapolating linearly to continuum. We observe that the $\beta_{\rm G} = 9$ result deviates less than 8% from the continuum limit in the range of temperatures studied. The lines are to guide the eye.

3.7 RESULTS

We concentrate on two physically significant observables, the sphaleron rate and the Higgs field expectation value as functions of temperature at $m_{\rm H} = 115\,{\rm GeV}$ and

$m_H = 160\,\mathrm{GeV}$. For both quantities we check for the finite volume and finite lattice spacing effects. Finally we implement the calculations for the Higgs mass $m_H = 125$ GeV.

3.7.1 *The Higgs field* $v(T)$

The gauge invariant Higgs condensate $\langle\phi^\dagger\phi\rangle$ is a direct probe of the phase transition or cross-over. At high temperatures it is close to zero, and at low temperatures it acquires an expectation value which grows as the temperature decreases. Because of the additive renormalisation, eq. (84), the symmetric-phase value can become negative. The results obtained at $\beta_G = 9$, lattice size 32^3, are shown in fig. 20 for $m_H = 115\,\mathrm{GeV}$ and 160 GeV. Note that $\langle\phi^2\rangle$ is in units of g^2T^2, and goes to infinity as temperature goes to zero.

At high temperature in the symmetric phase, $\langle\phi^\dagger\phi\rangle$ is close, but not quite equal, to zero. As the temperature is lowered, we enter the cross-over region where $\langle\phi^\dagger\phi\rangle$ grows rapidly. At smaller Higgs masses ($m_H \lesssim 72\,\mathrm{GeV}$), this rapid growth becomes a discontinuous jump, indicating a first-order transition, see fig. 11, [20]. Below the cross-over region, $\langle\phi^\dagger\phi\rangle/(g^2T^2)$ settles to an almost linear increase.

We then performed control simulations for $m_H = 115\,\mathrm{GeV}$ in order to check the validity of our results for the continuum limit ($a \to 0$) and the infinite- volume limit ($V \to \infty$). We measured $\phi^\dagger\phi$ at selected temperature values while varying the lattice spacing by more than a factor of two ($\beta_G = 6\ldots16$). The results are shown in fig. 22. In this case we can reliably take the continuum limit by linear extrapolation. We observe that when $\langle\phi^\dagger\phi\rangle$ is small, the cut-off effects are very small, and at the lowest temperatures studied $T \approx 130\,\mathrm{GeV}$ the $\beta_G = 9$ result deviates from the continuum limit by less than 8%. The physical volume was kept fixed, at $Lg_3^2 \approx 14$. We have checked that this is a large-enough volume so that the residual finite-volume effect is unobservable within our statistical accuracy.

3.7.2 *The sphaleron rate* $\Gamma_{\mathrm{sph}}(T)$

The sphaleron rate Γ/T^4 for Higgs masses 115 GeV and 160 GeV is shown in fig. 21, using $\beta_G = 9$ data. As expected, at high temperature in the symmetric phase, the rate becomes insensitive to the temperature apart from the trivial scaling. In this region the standard "canonical" real-time evolution is sufficient. As we proceed into the cross-over region there is a rather sharp turnover, with a drop of 10^{-3} over 5 GeV. In this region, both the canonical and multicanonical methods were used, and they agree very convincingly. Deeper in the broken phase, the decrease in the rate flattens out

somewhat to a clean exponential drop-off, and, using the multicanonical approach, we were able to follow the rate over 10 orders of magnitude. For comparison, we have included the extrapolation from [60], expected to be valid deep in the broken phase. We see that the slope is correct, but that the central value of the rate is off by about an order of magnitude; or equivalently that the temperature axis is shifted by about 2 GeV for a Higgs mass of 115 GeV and about 5 GeV in the 160 GeV case. The data are shown for $\beta_G = 9$, where the majority of our simulations were done.

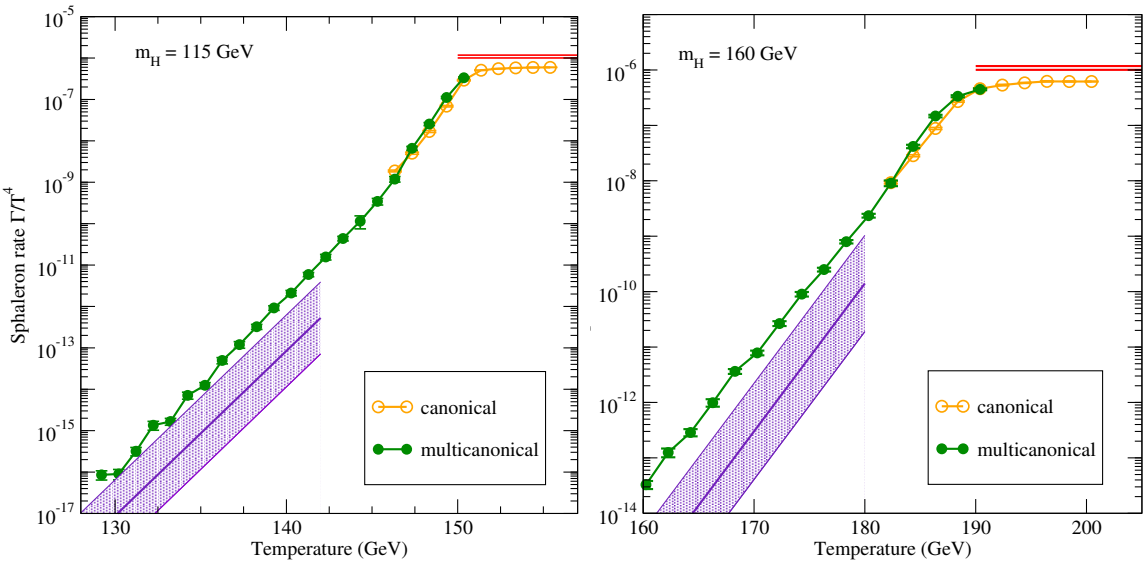

Figure 21: The sphaleron rate for $m_H = 115$ GeV (left) and 160 GeV (right) at $\beta_G = 9$. The shaded band is the theoretical estimate (plus error ranges extrapolated from lattice results in [50]) for the broken phase and the horizontal lines for the symmetric phase, as calculated in [60]. At high temperatures, the canonical and multicanonical results agree within errors.

Sphalerons are extended objects, and thus it is necessary to check the finite volume effects. Using a constant lattice spacing $\beta_G = 9$ and lattice sizes $L/a = 16$–54 we observed no systematic finite-size dependence within our statistical accuracy. Thus, we can be confident that $L = 32$, $a \approx 14/g_3^2$ is sufficiently large at all temperatures. This result is in agreement with ref. [61], where the volume dependence of the sphaleron rate became negligible at $L \gtrsim 5/g_3^2$ in pure SU(2) gauge theory.

As we did with the Higgs field expectation value, we investigated the dependence of the sphaleron rate on the lattice spacing. We chose a set of six temperatures in the interval 130-155 GeV and measured the rate at $\beta_G = 4/(g_3^2 a) = 6$–$16$, while keeping the physical volume approximately constant: $L \approx 3.5\beta_G = 14/g_3^2$. The lattice

spacings and volumes are shown in table 2, and the resulting sphaleron rates are shown in fig. 23.

In the symmetric phase the lattice-spacing dependence is very mild. Deep in the broken phase the rate appears to decrease as a is decreased. This can be understood in the light of the increasing Higgs field expectation value at smaller a, see fig. 22.

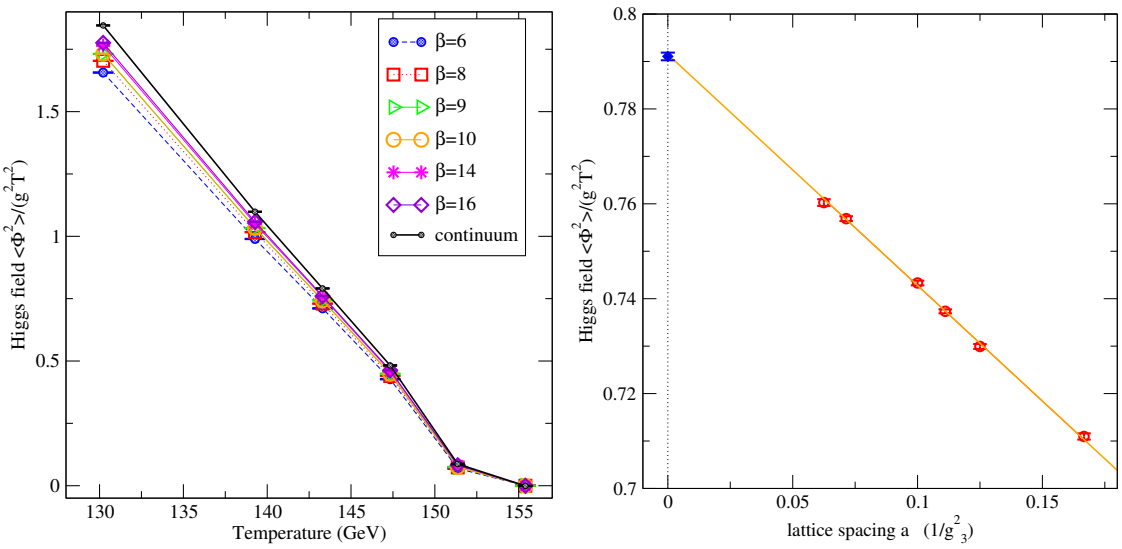

Figure 22: Left: the Higgs field calculated for $m_H = 115\,\mathrm{GeV}$ and several temperatures, with decreasing lattice spacing a, but keeping the volume constant, according to table 2. The black line is the continuum extrapolation. Right: an example of the continuum extrapolation at a single value of the temperature $T = 143\,\mathrm{GeV}$.

However, deep in the broken phase ($T \lesssim 145\,\mathrm{GeV}$) and for the smallest lattice spacings ($\beta_G \geqslant 14$) our multicanonical order parameter, cooled N_{CS} (fig. 15), becomes ineffective and we are not able to obtain a sufficiently accurate measurement of the rate for the proper continuum limit. This is due to the increased noise in the measurement at smaller lattice spacings: when the amplitude of the noise is of order unity, a large fraction of the configurations with (measured) N_{CS} near half-integer value are actually some distance from the top of the tunneling barrier. Thus, only a small fraction of these configurations will lead to tunneling trajectories.

The amount of noise can be reduced by applying more cooling before the measurement of N_{CS}. However, cooling evolves the configuration towards one of the vacua (integer N_{CS}), and with too much cooling the measured order parameter does not track the true Chern-Simons number well enough for effective update. We emphasize

$a\ (1/g_3^2)$	β_G	L	L/β_G
0.67	6	20	3.3
0.5	8	28	3.5
0.44	9	32	3.56
0.4	10	36	3.6
0.29	14	48	3.4
0.25	16	56	3.5

Table 2: Lattice values for the continuum limit. a is the lattice spacing, β_G is defined in eq. (81), L is the size of our volume. From the ratio L/β_G we notice that we keep the physical proportions constant, while we diminish the size of the lattice spacing a.

that despite these issues the multicanonical method remains exact in the limit of infinite statistics; it is only the efficiency of the method which suffers.

Because of this issue, our statistics at small lattice spacing is severely restricted and we cannot obtain a reliable continuum limit. Thus, our final answer remains the

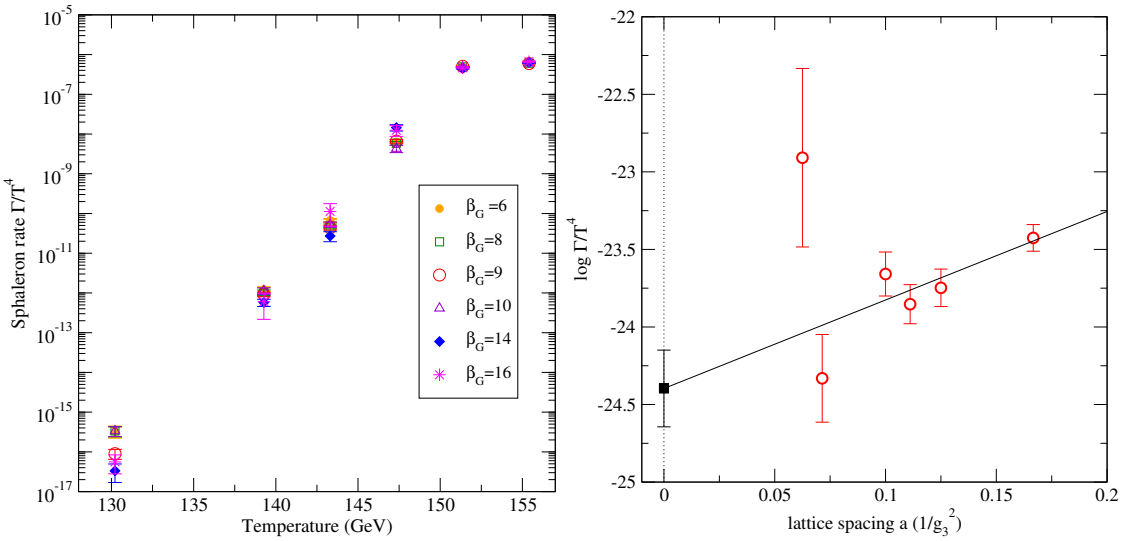

Figure 23: Left: the sphaleron rate calculated for $m_H = 115\,\mathrm{GeV}$ and with different lattice spacings a while keeping the physical volume constant. Right: an example of the rate at $T = 143\,\mathrm{GeV}$ as a function of the lattice spacing. Here the continuum limit has been extrapolated by assuming that the dominant error of $\log\Gamma$ is linear in a. However, if we extrapolate Γ itself linearly in a, the result is compatible with vanishing rate in the continuum limit.

$\beta_G = 9$ result, where we have most of the data. However, what the data indicates is that the true continuum limit is probably a factor of 2–3 below the $\beta_G = 9$ result deep in the broken phase, which very likely makes the agreement with ref. [60] in fig. 21 better.

3.7.3 *Results for the physical Higgs mass*

Recently, we have determined the sphaleron rate Γ/T^4 and the expectation value for the Higgs field $\langle\phi^2\rangle$ for the Higgs mass $m_H = 125\,\text{GeV}$. Figure 24 a) shows the Higgs field expectation value as a function of temperature. Again we start from the "symmetric phase" with canonical Monte Carlo simulations and lower the temperature to reach the "broken phase", where we switch to multicanonical simulations. We can see the Higgs field assuming a non-zero value when approaching the broken phase, and the transition between the two methods occurring smoothly.

The sphaleron rate as a function of temperature is shown in the lower plot of fig. 24. Here again we perform the simulations with canonical Monte Carlo at high temperatures and continue with multicanonical methods when reaching the cold broken phase. The sphaleron rate changes from its asymptotic value to become exponentially suppressed at very low temperatures. The canonical and multicanonical methods are in good agreement. The theoretical curves, used to compare our results, were obtained separately for the broken and symmetric phases, through perturbative calculations or by extrapolation from lattice simulations in [60].

3.8 LEPTOGENESIS

In baryogenesis via leptogenesis [62, 63], a lepton asymmetry is assumed to originate from some separate process, represented here by a time-dependent source $f_i(t)$ which may or may not be active at the electroweak scale. Sphaleron transitions equilibrate the system, so that the lepton asymmetry is transformed into net L_i and B. Following [60], the equations controlling this equilibration read

$$\dot{B}(t) = -\gamma(t)\left[B(t) + \eta(t)\sum_{i=0}^{n_G} L_i(t)\right], \tag{100}$$

$$\dot{L}_i(t) = -\frac{\gamma(t)}{n_G}\left[B(t) + \eta(t)\sum_{i=0}^{n_G} L_i(t)\right] + f_i(t), \tag{101}$$

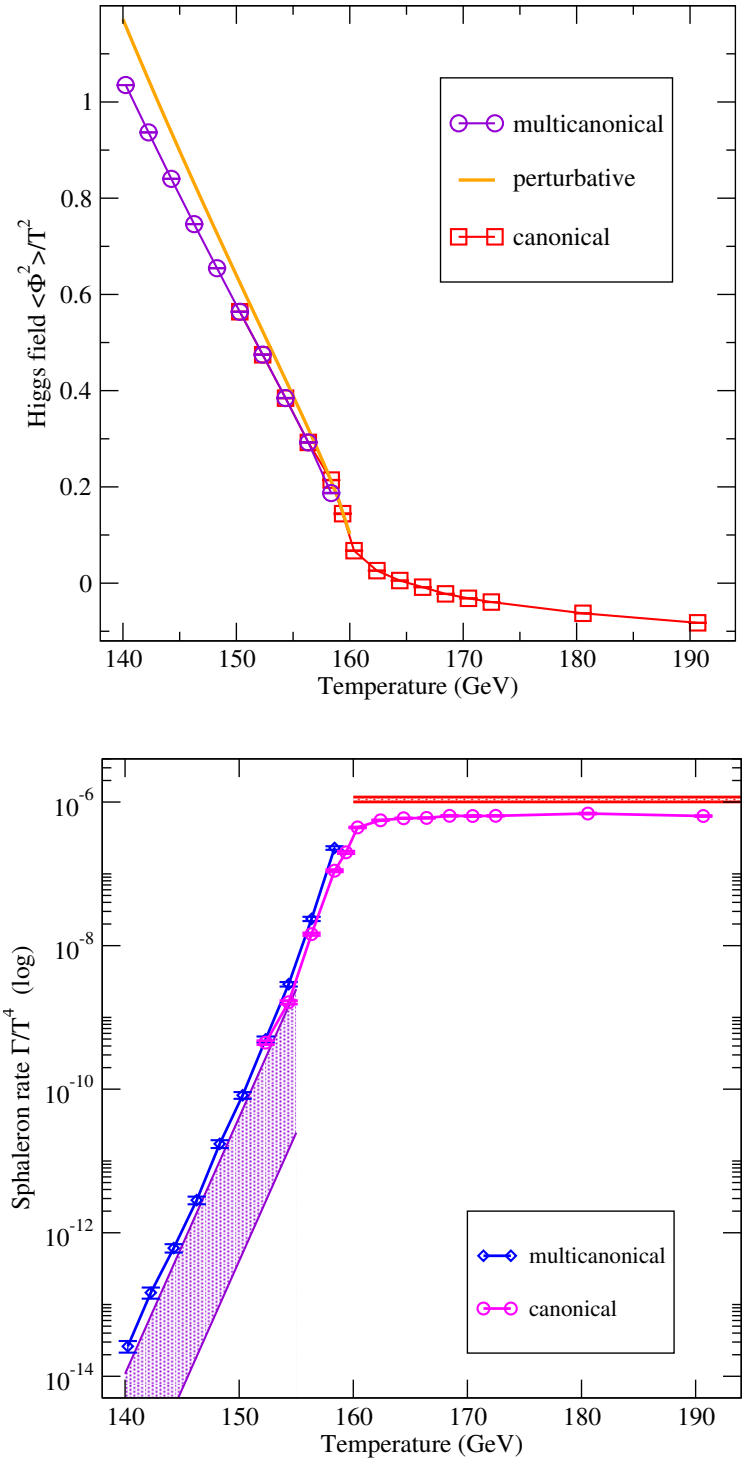

Figure 24: Top: The Higgs expectation value $\langle\phi^2\rangle$ for the Higgs mass of 125 GeV as a function of temperature. The high-temperature canonical and low- temperature multicanonical results match beautifully in the transition region. Bottom: The sphaleron rate for a Higgs mass of 125 GeV. The high-temperature canonical and low-temperature multicanonical results again match very well in the transition region. Also shown are previous high-temperature estimates $\sim 5 \times 10^{-7}\ T^4$, (top, horizontal line) and perturbative calculations in the low- temperature phase (bottom, wide band), both from [60].

where

$$\begin{aligned} T &= T(t), \\ \gamma(t) &= \gamma(\Gamma_{\rm sph}(T), v(T)), \\ \eta(t) &= \eta(v(T)) \\ n_G &= 3. \end{aligned} \tag{102}$$

Here $v(T)$ is the expectation value of the Higgs field, taken to be $v(T) \simeq \sqrt{\langle \phi^\dagger \phi \rangle}$.

As the sphaleron rate is well-known in the symmetric phase, we focus our interest on the cross-over region, to investigate the efficiency of lepton-to-baryon number conversion through the newly-calculated sphaleron rate. In order to enhance the effect of the sphaleron rate suppression at cross-over temperatures, we study the leptogenesis eqs. (100)–(101) in two limiting cases: one where the lepton-number source $f_i(t)$ was shut off well before the start of the cross- over, and one where we let the source active throughout.

We took $n_G = 3$ and assumed that all lepton species are equivalent $L_i = L$, $i = 1,2,3$, $\sum_i L_i = 3L$. The initial baryon and lepton numbers vanish $L(t_0) = B(t_0) = 0$. The source for the lepton number is therefore taken to be operational between $T = 200\,\text{GeV}$ and $T = T_{\rm cut-off}$,

$$f_i(t) = f(t) = \frac{f_0}{2}\left(1 - \tanh\left[\frac{T_{\rm cut-off} - T}{2\,\text{GeV}}\right]\right), \tag{103}$$

Since the equations are linear, the normalization of f_0 is arbitrary. This leaves only the source shut-off temperature $T_{\rm cut-off}$ as a free parameter, which we varied from 170 to 130 GeV, before and after the cross-over, respectively.

The full expressions for $\gamma(t)$ and $\eta(t)$ in eqs. (100)– (101) are [60]

$$\gamma(t) = n_G^2\,\rho\left(\frac{v(T)}{T}\right)\left[1 - \chi\left(\frac{v(T)}{T}\right)\right]\frac{\Gamma_{\rm sph}(T)}{T^3}, \qquad \eta(t) = \frac{\chi\left(\frac{v(T)}{T}\right)}{1 - \chi\left(\frac{v(T)}{T}\right)}, \tag{104}$$

where $T = T(t)$. The functions are defined as

$$\rho(x) = \frac{3\left[65 + 136 n_G + 44 n_G^2 + (117 + 72 n_G)x^2\right]}{2 n_G\left[30 + 62 n_G + 20 n_G^2 + (54 + 33 n_G)x^2\right]}, \tag{105}$$

$$\chi(x) = \frac{4\left[5 + 12 n_G + 4 n_G^2 + (9 + 6 n_G)x^2\right]}{65 + 136 n_G + 44 n_G^2 + (117 + 72 n_G)x^2}. \tag{106}$$

We calculated the evolution of lepton and baryon number from temperature 200 GeV down to 130 GeV. Using that to a good approximation in the early Universe $T \propto 1/a$, with $a(t)$ the scale factor, we have that

$$\frac{d}{dt} = -HT\frac{d}{dT}, \tag{107}$$

where H is the Hubble rate, given by the (radiation-dominated) Friedman equation[1]

$$H^2 = \frac{\pi^2 g^* T^4}{90 M_{pl}^2}, \quad g^* = 106.75, \quad M_{pl} = 2.43 \times 10^{18}\,\text{GeV}. \tag{108}$$

Over the range of temperatures used here, $H = (8.8 - 3.7) \times 10^{-14}$.

Once the source is turned off, and in the limit that L and B evolve much faster than ν and η, we can write the equations in terms of $Y = B + 3\eta L$

$$\frac{d\ln Y}{d\ln T} = \frac{\gamma(T)}{H(T)}\left(1 + \eta(t)\right), \tag{109}$$

so that $Y = 0$ is enforced unless γ/H is too small. Hence if the sphaleron rate is fast enough, we expect

$$-\frac{B(T)}{3L(T)\eta(T)} \simeq 1. \tag{110}$$

We say that the system is in "equilibrium" when this relation is obeyed. We note that $\eta\left(\nu(T)/T = 0\right) = 0.549...$ and $\eta\left(\nu(T)/T = \infty\right) = 0.48$.

The evolution of B and L in time is shown in fig. 25. Starting from zero at $T = 200\,\text{GeV}$, the introduction of the source leads to a growing L and, through sphaleron processes, growing B. This continues until the source is switched off; in the examples shown here $T_{\text{cut-off}} = 170\,\text{GeV}$ and $T_{\text{cut-off}} = 130\,\text{GeV}$. For the early cut-off, both B and L level off to some asymptotic value. But even without switching off the lepton source, at a temperature around 143 GeV the sphaleron rate becomes inefficient, and the baryon number levels off. Lepton number is still sourced, but no longer having B as a sink, the growth of L becomes steeper. $T_{\text{freeze-out}} = 143\,\text{GeV}$ corresponds to $\gamma(t)/H \simeq 10$, and $\nu(T)/T \simeq 0.5$.

What is perhaps more surprising is the ratio in eq. (110) when there is no source. Because the $\nu(t)$ increases through the transition, the equilibrium value $\eta(t)$ also changes (see inset in fig. 26). A large enough sphaleron rate relative to the Hubble rate would adjust B relative to L to accommodate this evolving "equilibrium", but as is

1 We ignored the effect of g^* changing slightly as the top quark begins acquiring its mass.

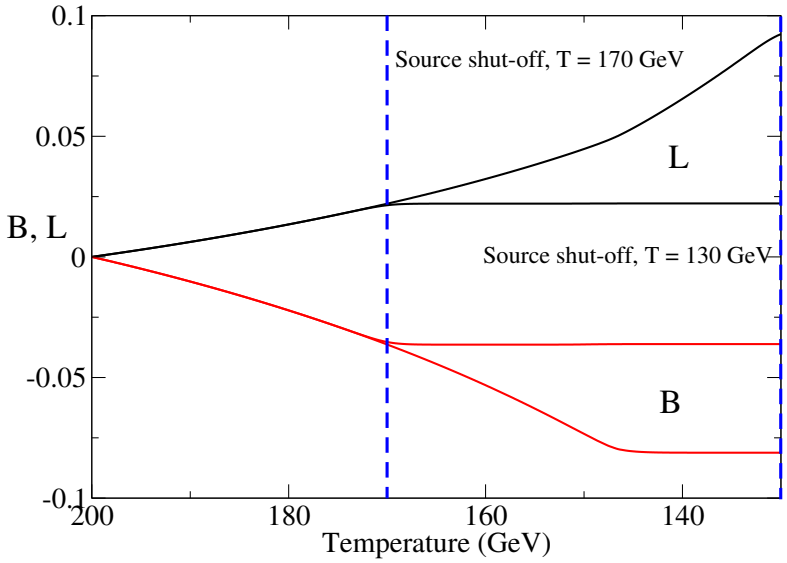

Figure 25: The evolution of baryon number B (red) and lepton number L (black) in the presence of a lepton number source, turned on at $T = 200\,\text{GeV}$. The source is turned off at $T = 170\,\text{GeV}$ and $130\,\text{GeV}$ respectively (blue dashed lines).

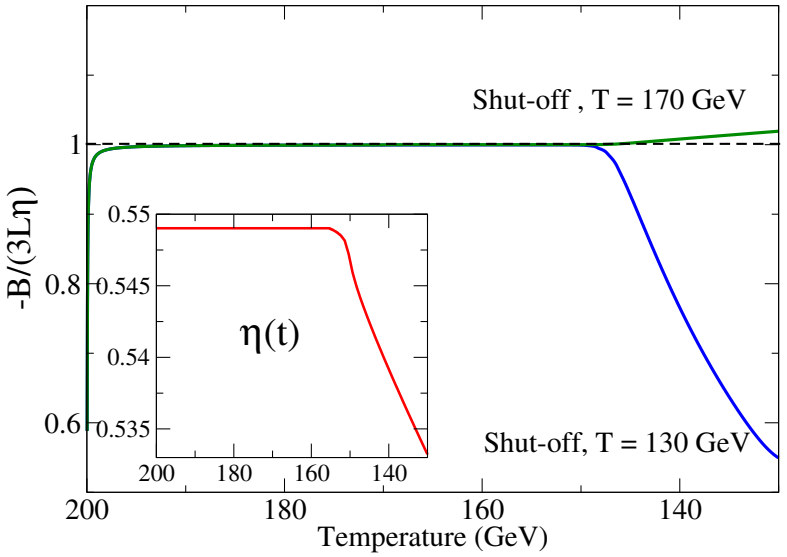

Figure 26: The evolution of the ratio (eq. (110)), with the source turned off at $T = 170$ GeV (green) and $130\,\text{GeV}$ (blue). Inserted: the evolution of the quantity $\eta(t)$.

clear from fig. 26, this does not happen. $\eta(t)$ just decreases and so the ratio becomes larger than 1. As a consequence, the asymptotic B and L obey

$$B(x=\infty) \simeq \eta(T_{\text{freeze-out}})3L(T_{\text{freeze-out}}) = 1.06 \times 3L(T_{\text{freeze-out}})\eta(x=\infty). \quad (111)$$

Figures 25 and 26 are based on the $m_H = 115\,\text{GeV}$ data. We did a similar calculation for the $m_H = 160\,\text{GeV}$ rate, giving the same picture but with $T_{\text{freeze-out}} = 175\,\text{GeV}$.

4 JET QUENCHING

The collision of high-energy partons produces jets of elementary particles and a hot and dense medium comparable to early Universe conditions. Jets have been observed at RHIC in proton-proton, deuteron-gold, and gold-gold collisions. The scattered quarks and gluons undergo large energy loss as they traverse the matter formed in the collision. This energy loss is called jet quenching. Jet quenching gives us a new way to probe the properties of the matter – the quark-gluon plasma – formed in these violent collisions.

4.1 HIGH-TEMPERATURE QCD

Deconfinement occurs at high pressures (e.g. neutron stars) or at high temperatures, producing the quark-gluon plasma (QGP), fig. 27. The presence of a phase transition is suggested by the increase in energy density, and subsequently in degrees of freedom, of strongly-coupled matter, at increasing temperatures. The critical temperature and the order of the transition depend very much on the quark content of the theory, as shown in fig. 28. For three families of massive quarks, the transition temperature is estimated to be [66]

$$T_c \approx 155 \text{ MeV}, \tag{112}$$

with critical energy density $\epsilon \approx 1.95$ GeV/ fm^{-3}, with respect to that of normal nuclear matter of $\epsilon \approx 0.15$ GeV/ fm^{-3}, see fig. 29. This critical temperature corresponds to a crossover.

Below the QCD scale $\Lambda_{QCD} \sim 200$ MeV, quarks are confined and the theory highly non-perturbative. In the quark-gluon plasma, significantly above the transition temperature, asymptotic freedom makes the strong coupling constant smaller, $\alpha_s \ll 1$. The system can then be treated perturbatively, see fig. 30.

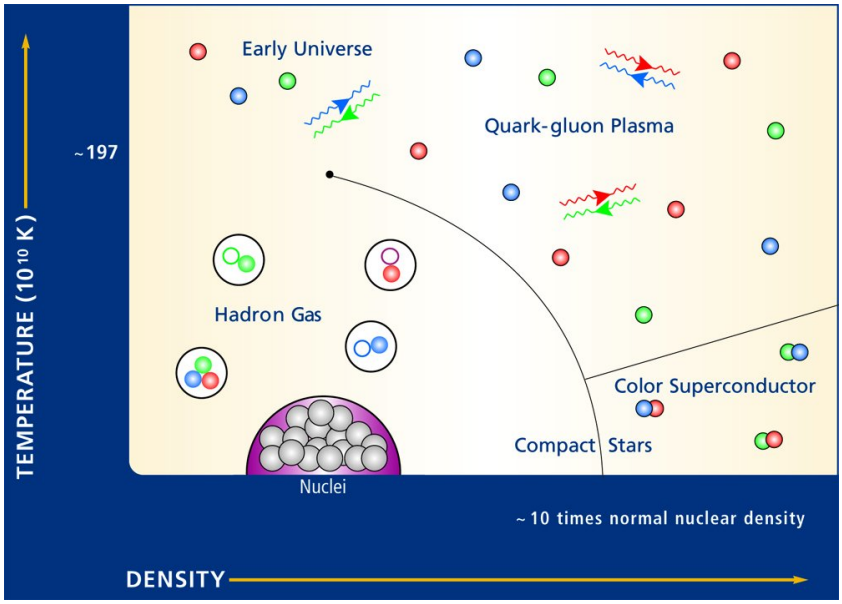

Figure 27: Phases of strongly-interacting matter, as a function of temperature and density [65]

To find an order parameter for the transition, we recall that above the critical temperature chiral symmetry is restored. The QCD Lagrangian is

$$\mathscr{L} = \bar{q}^i(i\gamma^\mu D_\mu - m_q)q^i - \frac{1}{4}F^a_{\mu\nu}F^{\mu\nu}_a \tag{113}$$

where

$$\begin{aligned} D^\mu &= \partial^\mu + igA^\mu_a\frac{\lambda^a}{2} \\ F^a_{\mu\nu} &= \partial_\mu A^a_\nu - \partial_\nu A^a_\mu - gf_{abc}A^b_\mu A^c_\nu, \end{aligned}$$

with coupling constant g, quarks q^i belonging to the SU(3) fundamental representation, gluon fields A^a_μ belonging to the adjoint one, and the 8 Gell-Mann 3×3-matrices λ^a, generators of the SU(3) in fundamental representation, satisfying $[\lambda_a,\lambda_b] = if_{abc}\lambda^c$. For massless quarks, the Lagrangian is invariant under global chiral transformations. The quark mass term in eq. (113) breaks explicitly the chiral symmetry. In particular, one can take the quark condensate $\langle\bar{q}q\rangle$ as an order parameter of the QCD transition:

$$\begin{aligned} \langle\bar{q}q\rangle &\approx 0 \qquad T > T_c \qquad \text{quark}-\text{gluon plasma} \\ \langle\bar{q}q\rangle &\neq 0 \qquad T < T_c \qquad \text{hadron gas.} \end{aligned}$$

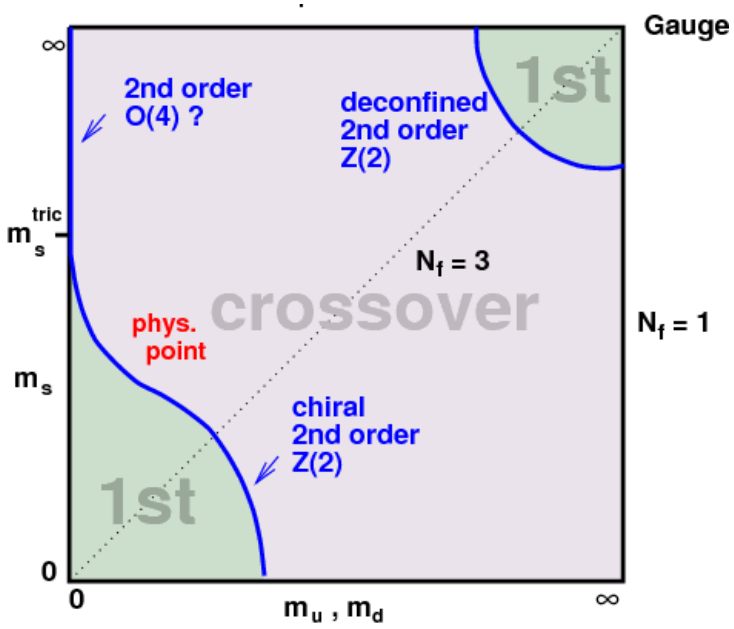

Figure 28: Order of the QCD phase transition is dependent on the quark masses [64].

The production of the quark-gluon plasma in heavy-ion collisions was first suggested in 1974 at the Bear Mountain workshop [67], and discovered at RHIC in 2005 [68]. The quark-gluon plasma forms in heavy-ion collisions when the energy density reaches values of the order of ~ 2 GeV/ fm^{-3}, then decouples and hadronizes at a time
~ 10 fm/c after the collision. There is therefore no direct way of observing the quark-gluon plasma, it must be probed with external sources. These are for example particles with high transverse momentum $p_\perp$, traveling through and interacting with the plasma. Jets forming at collision are the perfect probe. RHIC discovered that jets are quenched when traversing the plasma, that is they lose energy through gluon radiation. The scattering processes occurring while the hard probe traverses the medium are perturbative in nature [69].

4.2 THE EFFECTIVE THEORY

The properties of the quark-gluon plasma are described at the microscopic level by QCD at finite temperature, and by relativistic hydrodynamics at the macroscopic level. Indeed QGP behaves like a perfect fluid, with small ratio of viscosity over entropy density η/s due to the large number of degrees of freedom of the deconfined phase.

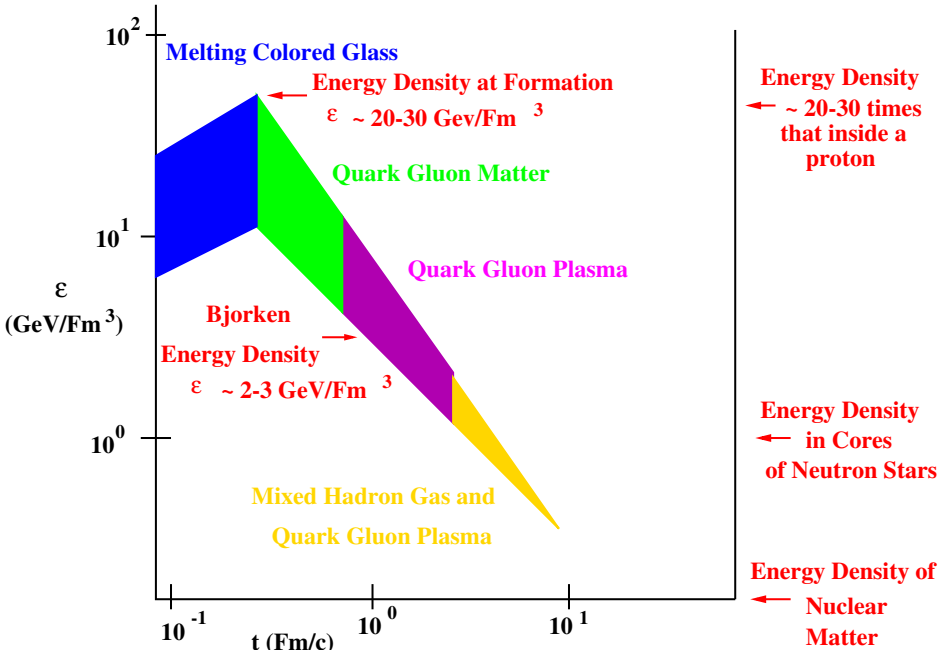

Figure 29: States of matter in heavy-ion collisions shown in terms of energy density as a function of time [70].

In finite-temperature field theory, configurations evolve in imaginary time $\tau = -it$, with $0 \leqslant \tau \leqslant \beta$, where $\beta = 1/T$. This allows to use ordinary quantum field theory with a Euclidean metric. In momentum space, continuous frequencies are substituted by discrete ones, the Matsubara frequencies for bosonic and fermionic fields

$$\begin{aligned} k_0^{\text{boson}} &= \frac{2\pi n}{\beta} \\ k_0^{\text{fermion}} &= \frac{(2n+1)\pi}{\beta} \end{aligned} \tag{114}$$

with $n \in Z$.

We impose periodic conditions for bosonic fields

$$\phi(1/T, \vec{x}) = \phi(0, \vec{x}). \tag{115}$$

For fermion fields, the boundary conditions are antiperiodic.

Finite-temperature perturbation theory can be used only for small coupling constant values, $\alpha_s \lesssim 0.1$, $T \gg T_c$, which is the case we want to approximate to our deconfined QGP. With large coupling constant, there are large $\mathcal{O}(g)$ corrections, which come from classical non-abelian plasma effects.

At high temperatures, QCD has three scales: the ultrasoft $\sim g^2T/\pi$, the soft $\sim gT$, and the hard modes $\sim \pi T$. It has been shown [40, 41] that it is possible to study the hard and soft modes separately. As hard modes behave perturbatively well [71, 72], they can be integrated out and we are left with a three-dimensional effective theory, EQCD, the electrostatic QCD, describing the soft scale, see fig. 30.

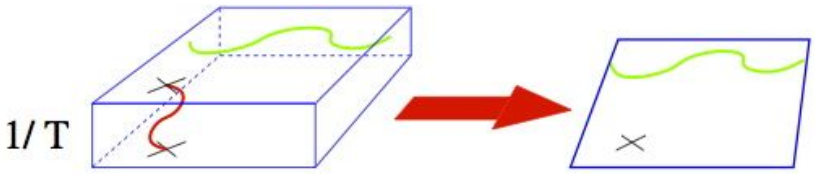

Figure 30: QCD dimensional reduction (illustration from [73]).

Large corrections are expected also for real-time quantities, some of which (collision kernel $C(q_\perp)$, momentum broadening coefficient $\hat{q}$) have been calculated in the EQCD framework [74]. For other real-time quantities though, a dimensionally-reduced theory has not been fully developed yet, and other effective theories need to be used.

4.3 WILSON LINE

The propagation of a sufficiently high-energy excitation through the medium can be described in terms of a null Wilson line, and the transverse-momentum exchange with the medium is related to the falloff with distance of a parallel pair of such lines [75, 76]. Specifically, the probability per length to exchange transverse momentum $\Delta p_\perp$ is given by

$$\frac{(2\pi)^2 d\Gamma}{d^2\Delta p_\perp\, dt} \equiv C(p_\perp), \qquad C(p_\perp) = \int d^2x_\perp e^{i\mathbf{p}_\perp\cdot\mathbf{x}_\perp} C(x_\perp). \tag{116}$$

$C(x_\perp)$ is determined by a Wilson loop with two null segments of length l and two transverse spatial components of length $x_\perp$:

$$\begin{aligned} C(x_\perp) &= \lim_{l\to\infty} -\frac{1}{\ell} \ln \mathrm{Tr}\, W_{l\times x_\perp}, \\ W_{l\times x_\perp} &= \langle U_{(0,0,0);(l,0,l)} U_{(l,0,l);(l,\mathbf{x}_\perp,l)} U_{(l,\mathbf{x}_\perp,l);(0,\mathbf{x}_\perp,0)} U_{(0,\mathbf{x}_\perp,0);(0,0,0)} \rangle, \end{aligned} \tag{117}$$

where $U_{x^\mu;y^\mu}$ are straight Wilson lines from x^μ to y^μ, and the three entries are the time, transverse coordinate, and longitudinal coordinate. The Wilson loop is to be evaluated in the density matrix describing the collision, which is presumably a thermal density matrix. Knowledge of $C(p_\perp)$, or equivalently $C(x_\perp)$, is a key input into models of medium-induced jet energy loss and jet modification [76, 77].

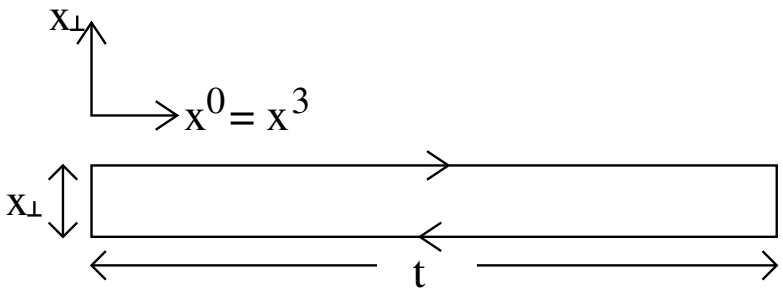

Figure 31: A long, thin rectangular Wilson loop stretching along the light-cone coordinate x_+, with a small transverse extension $x_\perp$ [74].

The jet quenching parameter

$$\hat{q} = \frac{\langle p_\perp^2 \rangle}{l} \tag{118}$$

can be evaluated in terms of the collision kernel $C(p_\perp)$ of eq. (116)

$$\hat{q} = \int \frac{d^2p_\perp}{(2\pi)^2}\, p_\perp^2\, C(p_\perp). \tag{119}$$

The leading order perturbative form of $C(p_\perp)$ is fully known [78], and for momentum transfers of order of the temperature or higher $p_\perp \gtrsim T$, the corrections to the leading order result are suppressed by $\mathcal{O}(g^2)$. For a soft momentum transfer $p_\perp \sim gT$, however, the introduction of a soft scale forces one to use resummed perturbation theory, and the next-to-leading order correction arises already at the $\mathcal{O}(g)$-relative order, making the physics of soft momentum transfers significantly more complicated.

However, Caron-Huot has shown [74] that for soft momentum transfers, to NLO, the Wilson loop $W_{l\times x_\perp}$ above can be replaced by a Wilson loop in the much simpler theory of EQCD, that is, QCD dimensionally reduced to three Euclidean dimensions, with the A^0 field converted into an adjoint scalar field Φ, where, roughly speaking,

$$g_{3d}\Phi = iA^0 \qquad \text{and} \qquad g_{3d}^2 \sim g^2 T.$$

Specifically, we have

$$W_{\ell\times x_\perp} \to \tilde{U}_{(0,0);(0,l)} U_{(0,l);(\mathbf{x}_\perp,l)} \tilde{U}_{(\mathbf{x}_\perp,l);(\mathbf{x}_\perp,0)} U_{(\mathbf{x}_\perp,0);(0,0)}\,. \tag{120}$$

There is now no time coordinate, only the transverse and z coordinates. The complication is that the Wilson lines which replace the null lines in the 4D version of W are modified, still containing the descendant of the A^0 field, which enters into the definition of $\tilde{U}$:

$$\tilde{U}_{(0,0);(0,l)} = \mathrm{Pexp}\int_0^l dz\, T_a (iA_z^a + g\Phi^a)\,. \tag{121}$$

The representation matrices T_a should be in the same representation as the propagating particle, which we will label R (fundamental or adjoint representation). The relative phase – A_z enters with an i and Φ does not – is because Φ is a Euclidean continuation of A^0 and the i factor is absorbed in the Wick rotation. The overall sign is reversed in $\tilde{U}_{(\mathbf{x}_\perp,l);(\mathbf{x}_\perp,0)}$. We will call this modified Wilson line the null Wilson line of EQCD.

Perturbation theory fails near the QCD crossover because the theory is genuinely strongly coupled there. It is, however, possible that the failure of perturbation theory at a few times the crossover temperature arises because the 3D theory is strongly coupled, while the short-distance physics involved in dimensional reduction is not [72]. In this case, a non-perturbative treatment of the 3D theory may still give useful information about QCD at the highest temperatures achieved in heavy ion collisions. If true, then the non-perturbative nature in the interaction of a jet parton with the medium is captured by the EQCD value of $C(p_\perp)$, which can be measured on the lattice. With this motivation, there has been an upswing in interest, recently, in studying the Wilson loop and $C(x_\perp)$ in EQCD on the lattice [79]. The relation between continuum thermal QCD and continuum EQCD is known to high perturbative order [72, 80–82], and the matching of the action, and some operators, between continuum and lattice EQCD is known to order $g_{3d}^2 a$ [83]. But the Wilson line in eq. (121) is a new operator and its lattice implementation has not been studied beyond the tree level. In practice it is challenging to make lattice studies quantitatively reliable without a calculation of the $\mathcal{O}(g_{3d}^2 a)$ renormalization of the null Wilson line operator. This is true even if the lattice spacing is taken to be very small, if one is simultaneously interested in $C(x_\perp)$ at short distances. Indeed, the first efforts to numerically determine the $C(p_\perp)$ by Panero, Rummukainen, and Schäfer [79] show how it is challenging to make contact with perturbation theory at $p_\perp \gg gT$, corresponding to small spatial separations. Therefore a study of $\mathcal{O}(a)$ corrections to the null Wilson line operator are essential to the success of this program.

4.4 STATEMENT OF THE PROBLEM

4.4.1 *Lattice and continuum action*

EQCD is the theory of a three-dimensional SU(N) gauge field A^i with field strength $F^{ij} \equiv F_a^{ij} T^a$, together with an adjoint scalar $\Phi \equiv \Phi^a T_a$ (with T_a the fundamental representation group generators normalized such that $\mathrm{Tr}\, T_a T_b = \delta_{ab}/2$). Writing

the path integral as $\int \mathscr{D}[A,\Phi]\exp(-S_{\rm EQCD})$, the most general super-renormalizable action in the continuum is

$$S_{\rm EQCD,c} = \int d^3x \left(\frac{1}{2g_{3d}^2} \mathrm{Tr}\, F^{ij}F^{ij} + \mathrm{Tr}\, D^i\Phi D^i\Phi + m_D^2 \mathrm{Tr}\,\Phi^2 + \lambda_1 (\mathrm{Tr}\,\Phi^2)^2 + \lambda_2 \mathrm{Tr}\,\Phi^4 \right), \tag{122}$$

where we have not shown the counterterm which subtracts UV divergences from the $\mathrm{Tr}\,\Phi^2$ term. The three-dimensional theory corresponds to the dimensionally-reduced four-dimensional QCD along a *matching curve*, specifying the values of the parameters of EQCD as a function of four-dimensional parameters: g, T, N and the number and masses of quark species N_f and m_i. Explicit expressions can be found in eqs. (5.2)-(5.5) of [84]. The quark mass dependence is discussed in [85].

It is customary to introduce dimensionless versions of the mass and scalar coupling terms, by defining[1]

$$y \equiv \frac{m_D^2[\mu_{\overline{\rm MS}} = g_{3d}^2]}{g_{3d}^4}, \qquad x_1 = \frac{\lambda_1}{g_{3d}^2}, \qquad x_2 = \frac{\lambda_2}{g_{3d}^2}. \tag{123}$$

The corresponding lattice theory, with lattice spacing a, is defined in terms of the link matrices $U_i(x) = U_{x;x+a\hat{i}}$ and the lattice scalar field Φ_L. The lattice action is

$$\begin{aligned} S_{\rm EQCD,L} &= \frac{2N}{Z_g g_{3d}^2 a} \sum_{x,ij} \left(1 - \frac{1}{N}\mathrm{Tr}\,\Box_{x,ij}\right) \\ &\quad + 2Z_\Phi \sum_{x,i} \mathrm{Tr}\left(\Phi_L^2(x) - \Phi_L(x)U_i(x)\Phi_L(x+a\hat{i})U_i^\dagger(x)\right) \\ &\quad + \sum_x Z_4 \left[(x_1+\delta x_1)\,\mathrm{Tr}\,\Phi_L^4 + (x_2+\delta x_2)\left(\mathrm{Tr}\,\Phi_L^2\right)^2\right] + Z_2(y+\delta y)\,\mathrm{Tr}\,\Phi_L^2, \end{aligned} \tag{124}$$

$$\Box_{x,ij} \equiv U_i(x)U_j(x+a\hat{i})U_i^\dagger(x+a\hat{j})U_j^\dagger(x), \tag{125}$$

and the lattice implementation of $\tilde{U}$ is

$$\tilde{U}_{(0,0);(0,na)} = \prod_{m=0}^{n-1} \exp\left(ZT_R^a \Phi_L^a(ma\hat{z})\right) U_{z,R}(ma\hat{z}), \tag{126}$$

for a Wilson line in the R representation. Note that there is no factor of i in $\exp(Z\Phi_L)$, which is not a unitary matrix.

1 For SU(2) or SU(3), the $\mathrm{Tr}\,\Phi^4$ and $(\mathrm{Tr}\,\Phi^2)^2$ terms are not independent, as $\mathrm{Tr}\,\Phi^4 = (\mathrm{Tr}\,\Phi^2)^2/2$ for these groups. In these cases one of the scalar terms can be eliminated in favor of the other.

Figure 32: Diagrams giving rise to the leading-order contribution to $C(x_\perp)$. Two Wilson lines (solid) are shown with the exchange between lines of an A field (wiggly) or a Φ field (dashed).

The value of the scalar field wave function normalization Z_Φ is actually a free choice in implementing the lattice theory, corresponding to the normalization choice for the lattice scalar field. We focus on the combinations Z_g, Z^2/Z_Φ, Z_2/Z_Φ, and Z_4/Z_Φ^2, which are invariant under this normalization freedom. At tree level we would have

$$\begin{aligned} Z_g &= 1 \\ \frac{Z^2}{Z_\Phi} &= g_{3d}^2 a = \frac{Z_4}{Z_\Phi^2} \\ \frac{Z_2}{Z_\Phi} &= g_{3d}^4 a^2. \end{aligned}$$

The coefficients Z_g, Z_2/Z_Φ, Z_4/Z_Φ^2, $\delta x_{1,2}$ and δy are already known. Our goal is to determine the remaining unknown parameter Z^2/Z_Φ, which controls the renormalization of the null Wilson line of EQCD.

4.4.2 *Sensitivity of Wilson loop to renormalization*

Since we are interested in the l-dependence of $\mathrm{Tr}\,W$ when l is large, we can ignore contributions from the ends and corners of the Wilson loop and focus on correlations between the long edges. We are also only interested in the $x_\perp$-dependence of $C(x_\perp)$, since any $x_\perp$-independent piece does not enter in $C(p_\perp)$. Therefore we need only consider diagrams with at least one line connecting the null Wilson lines. At lowest order there are two, involving the exchange of an A_z or a Φ line, as illustrated in fig. 32. Because the A_z fields attach with factors of $i, -i$ while the Φ fields attach with factors of $1, -1$, the contributions are of opposite sign. In the continuum they are

$$\begin{aligned} C_{LO}(x_\perp) &= \int_{-\infty}^{\infty} dz \langle A_z(x_\perp, z) A_z(0) - g_{3d}^2 \Phi(x_\perp, z)\Phi(0)\rangle \\ \Rightarrow \quad \frac{C(p_\perp)}{C_R} &= \frac{g_{3d}^2}{p_\perp^2} - \frac{g_{3d}^2}{p_\perp^2 + m_D^2}, \end{aligned} \tag{127}$$

while on the lattice we find (defining, as usual $U_i(x) \approx (1 + iaA_i(x + a\hat{i}/2))$)

$$\begin{aligned} C_{LO}(x_\perp) &= \frac{1}{a}\sum_n \langle a^2 A_z(x_\perp, na) A_z(0) - Z^2 \Phi(x_\perp, na)\Phi(0)\rangle \\ \Rightarrow \quad \frac{C(p_\perp)}{C_R} &= \frac{Z_g g^2}{\tilde{p}_\perp^2} - \frac{Z^2/aZ_\Phi}{\tilde{p}_\perp^2 + m_D^2}. \end{aligned} \tag{128}$$

Here $\tilde{p}_x^2 \equiv \sin^2(p_x a/2)/(a/2)^2$ is the lattice momentum and C_R is the quadratic Casimir in the representation R of the Wilson loop.

The important feature of eq. (127) is that the two terms approximately cancel at large $p_\perp$, up to subleading $m_D^2/p_\perp^4$ corrections. The presence of the lattice propagator in eq. (128) does not change this cancellation. Of course this cancellation does not persist at higher loop order, but because the theory is super-renormalizable, each loop order gives weaker large-$p_\perp$ behavior. Indeed, at NLO the large $p_\perp$ behavior is $\mathcal{O}(g_{3d}^4/p_\perp^3)$ [74].

The problem is that the renormalization of Z – which is not taken into account in a lattice calculation – will spoil the cancellation in eq. (128), giving rise to uncanceled $1/p_\perp^2$ large-$p_\perp$ behavior. Therefore the short-distance or large-$p_\perp$ behavior is especially sensitive to errors in the Wilson line renormalization constant Z. The need to renormalize the Wilson line operator increases at small separation, scaling as the inverse separation of the Wilson lines in lattice units. For instance, if the Wilson lines are separated by N lattice spacings in the transverse direction, the $\mathcal{O}(a)$ corrections are $\mathcal{O}(1/N)$, no matter how small the lattice spacing may be. Finding the $\mathcal{O}(a)$ correction to Z will improve this behavior to $1/N^2$, an important correction for realistic values $N \sim 5$.

4.5 CALCULATION STRATEGY

The matching calculation consists of computing $C(p_\perp)/C_R$ at NLO within continuum and lattice EQCD, and fixing the coefficients of the lattice theory such that the calculations agree to all orders in g_{3d} and λ_i and up to the desired order in a, here $\mathcal{O}(a)$. As usual, once the coefficients are fixed at one order, the infrared behavior is automatically the same at the next order, since the infrared behaviors of the theories coincide by construction. Then it is the difference in the ultraviolet region of any loops which must be calculated. As usual, such behavior can be understood in terms of a renormalization of the parameters of the theory appearing in diagrams of lower order.

Again we only need diagrams with at least one line running between the null Wilson lines. There are a number of NLO diagrams, see fig. 33. Fortunately, both propagators in diagrams A and B must be infrared (since they connect spatially well-separated

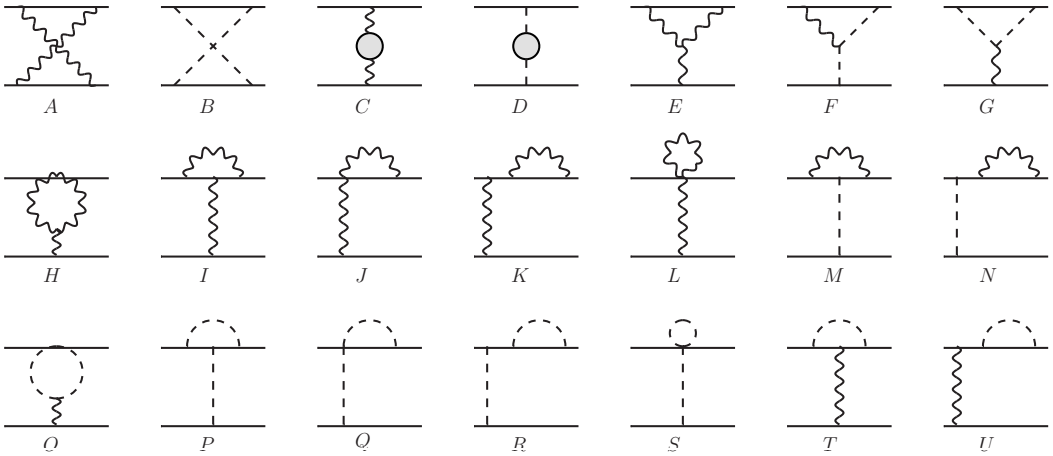

Figure 33: Diagrams needed at next-to-leading order. Solid lines are the Wilson lines, wiggly lines are A fields, dashed lines are Φ fields, blobs are self-energies. Each diagram implicitly also represents the same diagram reflected right-left or top-bottom.

Wilson lines), so they do not contribute to UV renormalization. In Feynman gauge (which we will use throughout), diagrams E, H, and O are zero. Diagrams J, L, Q, S have no continuum analog; they arise because $U_z = \exp(ia A_z)$ and $\exp(Z\Phi)$ are nonlinear in A_z and Φ. But the form of the lattice Wilson line, eq. (126), does not contain anything which would introduce mixed A_z, Φ vertices on the Wilson line, so there are no mixed-field analogs of diagrams H, J, L, O, Q, S.

Since only the UV behavior of diagrams is relevant, we can ignore m_D and treat the propagators to be

$$\langle A_z A_z(p)\rangle = \frac{Z_g g_{3d}^2}{\tilde{p}^2}, \qquad \langle \Phi_L \Phi_L(p)\rangle = \frac{a Z_\Phi^{-1}}{\tilde{p}^2}. \tag{129}$$

In this case, for soft momenta $p_\perp \ll 1/a$ running between the Wilson lines, we extract all $1/p_\perp^2$ contributions, and choose the value of Z^2/Z_Φ such that they cancel, as they do in the continuum according to eq. (127).

4.6 RESULT

We have found the 1-loop renormalization factor which should be included in the lattice implementation of the EQCD null Wilson line. Specifically, given the definition of the lattice action found in eq. (124) and of the Wilson line operator in eq. (126),

the ratio of the normalization of the lattice scalar field Φ_L appearing in the Wilson line to its normalization in the action is

$$\frac{Z^2}{Z_\Phi a} = 1 + \frac{g_{3d}^2 a C_A}{4}\left(\frac{4}{3}\frac{\Sigma}{4\pi} - 16\frac{\xi}{4\pi}\right), \tag{130}$$

where the constants appearing here are are

$$\frac{\Sigma}{4\pi a} \equiv \int_{-\pi/a}^{\pi/a} \frac{d^3p}{(2\pi)^3}\frac{1}{\tilde{p}^2}, \qquad \frac{\xi a}{4\pi} \equiv \int_{-\pi/a}^{\pi/a} \frac{d^3p}{(2\pi)^3}\frac{1}{(\tilde{p}^2)^2} - \int_{-\infty}^{\infty} \frac{d^3p}{(2\pi)^3}\frac{1}{(p^2)^2}, \tag{131}$$

numerically $\xi = 0.152859324966101$ and $\Sigma = 3.17591153562522$. This constitutes our main result.

Using this renormalization in the Wilson line will facilitate faster and more accurate lattice calculations of the infrared contribution to $\hat{q}$ and $C(p_\perp)$. In particular, it eliminates the last source of error (except for δy) which obstructs a quick and accurate continuum extrapolation in the lattice determination of $C(x_\perp)$.

[1] A. H. Guth, Phys. Rev. D **23** (1981) 347.

[2] P. A. R. Ade *et al.* [Planck Collaboration], arXiv:1303.5086 [astro-ph.CO].

[3] J. Preskill, Phys. Rev. Lett. **43** (1979) 1365.

[4] S. Watson, astro-ph/0005003.

[5] D. H. Lyth, D. Wands, Phys. Lett. **B524** (2002) 5-14. [hep-ph/0110002].

[6] S. Mollerach, Phys. Rev. D **42** (1990) 313.

[7] K. Enqvist, R. N. Lerner and O. Taanila, JCAP **1112** (2011) 016 [arXiv:1105.0498 [astro-ph.CO]].

[8] S. R. Coleman, E. J. Weinberg, Phys. Rev. **D7** (1973) 1888-1910.

[9] M. H. Thoma and C. T. Traxler, Phys. Lett. B **378** (1996) 233 [hep-ph/9601254].

[10] J. H. Traschen and R. H. Brandenberger, Phys. Rev. D **42** (1990) 2491.

[11] L. Kofman, A. D. Linde and A. A. Starobinsky, Phys. Rev. Lett. **73** (1994) 3195 [hep-th/9405187].

[12] A. Rajantie and E. J. Copeland, Phys. Rev. Lett. **85** (2000) 916 [hep-ph/0003025].

[13] A. R. Liddle and D. H. Lyth, Cambridge, UK: Univ. Pr. (2000) 400 p.

[14] A. Chambers, S. Nurmi, A. Rajantie, JCAP **1001** (2010) 012. [arXiv:0909.4535 [astro-ph.CO]].

[15] P. A. R. Ade *et al.* [Planck Collaboration], arXiv:1303.5084 [astro-ph.CO].

[16] P. A. R. Ade *et al.* [Planck Collaboration], arXiv:1303.5082 [astro-ph.CO].

[17] V. A. Kuzmin, V. A. Rubakov and M. E. Shaposhnikov, Phys. Lett. B **155** (1985) 36.

[18] G. Culligan, S. G. F. Frank, and J. R. Holt, Proceedings of the Physical Society, 73, (1959)169.

[19] N. Turok, "The primordial universe. Proceedings, Summer School on physics, 71st session, Les Houches, France, June 28-July 23, 1999".

[20] K. Kajantie, M. Laine, K. Rummukainen and M. E. Shaposhnikov, Phys. Rev. Lett. **77** (1996) 2887 [hep-ph/9605288].

[21] K. Rummukainen, Nucl. Phys. Proc. Suppl. **53** (1997) 30 [hep-lat/9608079].

[22] M. Laine and K. Rummukainen, Nucl. Phys. Proc. Suppl. **73** (1999) 180 [hep-lat/9809045].

[23] J. S. Bell and R. Jackiw, Nuovo Cim. A **60** (1969) 47.

[24] S. L. Adler, Phys. Rev. **177** (1969) 2426.

[25] A. A. Belavin, A. M. Polyakov, A. S. Schwartz and Y. .S. Tyupkin, Phys. Lett. B **59** (1975) 85.

[26] G. 't Hooft, Phys. Rev. Lett. **37** (1976) 8.

[27] G. 't Hooft, Phys. Rev. D **14** (1976) 3432 [Erratum-ibid. D **18** (1978) 2199].

[28] V. A. Rubakov and M. E. Shaposhnikov, Usp. Fiz. Nauk **166** (1996) 493 [Phys. Usp. **39** (1996) 461] [hep-ph/9603208].

[29] G. D. Moore, Phys. Rev. D **62**, 085011 (2000) [arXiv:hep-ph/0001216].

[30] J. M. Cline, hep-ph/0609145.

[31] K. Kajantie, M. Laine, K. Rummukainen and M. E. Shaposhnikov, Nucl. Phys. **B458** (1996) 90-136. [hep-ph/9508379].

[32] F. R. Klinkhamer and N. S. Manton, Phys. Rev. D **30** (1984) 2212.

[33] P. B. Arnold and L. D. McLerran, Phys. Rev. D **36** (1987) 581.

[34] L. Carson, X. Li, L. D. McLerran and R. -T. Wang, Phys. Rev. D **42** (1990) 2127.

[35] J. Baacke and S. Junker, Phys. Rev. D **49** (1994) 2055 [hep-ph/9308310].

[36] J. Baacke and S. Junker, Phys. Rev. D **50** (1994) 4227 [hep-th/9402078].

[37] A. D. Linde, Phys. Lett. **B96** (1980) 289.

[38] K. Farakos, K. Kajantie, K. Rummukainen and M. E. Shaposhnikov, Nucl. Phys. **B425** (1994) 67-109. [hep-ph/9404201].

[39] K. Farakos, K. Kajantie, K. Rummukainen and M. E. Shaposhnikov, Nucl. Phys. **B442** (1995) 317-363. [hep-lat/9412091].

[40] P. H. Ginsparg, Nucl. Phys. B **170** (1980) 388.

[41] T. Appelquist and R. D. Pisarski, Phys. Rev. **D23** (1981) 2305.

[42] S. Nadkarni, Phys. Rev. **D27** (1983) 917.

[43] N. P. Landsman, Nucl. Phys. **B322** (1989) 498.

[44] A. Jakovac, K. Kajantie and A. Patkos, Phys. Rev. **D49** (1994) 6810-6821. [hep-ph/9312355].

[45] E. Braaten and A. Nieto, Phys. Rev. D **51** (1995) 6990 [hep-ph/9501375].

[46] K. Kajantie, M. Laine, K. Rummukainen and M. E. Shaposhnikov, Nucl. Phys. **B466** (1996) 189-258. [hep-lat/9510020].

[47] M. Laine, Nucl. Phys. **B451** (1995) 484-504. [hep-lat/9504001].

[48] J. Ambjorn and A. Krasnitz, Nucl. Phys. B **506**, 387 (1997) [arXiv:hep-ph/9705380].

[49] W. H. Tang and J. Smit, Nucl. Phys. B **482** (1996) 265 [arXiv:hep-lat/9605016].

[50] G. D. Moore, Phys. Rev. D **59**, 014503 (1999) [arXiv:hep-ph/9805264].

[51] D. Bödeker, L. McLerran and A. Smilga, Phys. Rev. D **52** (1995) 4675 [hep-th/9504123].

[52] P. Arnold, D. Son and L.G. Yaffe, Phys. Rev. **D55**, 6264 (1997) [hep-ph/9609481].

[53] E. Braaten and R. Pisarski, Nucl. Phys. **B337**, 569 (1990); J. Frenkel and J. Taylor, Nucl. Phys. **B334**, 199 (1990); J. Taylor and S. Wong, Nucl. Phys. **B346**, 115 (1990); J. Frenkel and J. Taylor, Nucl. Phys. **B 374**, 156 (1992); E. Braaten and R. Pisarski, Phys. Rev. **D 45**, 1827 (1992); J. P. Blaizot and E. Iancu, Phys. Rev. Lett. **70**, 3376 (1993) [hep-ph/9301236]; Nucl. Phys. **B417**, 608 (1994) [hep-ph/9306294]; V.P. Nair, Phys. Rev. **D48**, 3432 (1993) [hep-ph/9307326].

[54] G. D. Moore, C. R. Hu and B. Muller, Phys. Rev. D **58**, 045001 (1998) [arXiv:hep-ph/9710436].

[55] D. Bodeker, G. D. Moore and K. Rummukainen, Phys. Rev. D **61** (2000) 056003 [arXiv:hep-ph/9907545].

[56] D. Bodeker, Phys. Lett. B **426** (1998) 351 [arXiv:hep-ph/9801430].

[57] P. B. Arnold and L. G. Yaffe, Phys. Rev. D **62** (2000) 125014 [arXiv:hep-ph/9912306].

[58] G. D. Moore, Nucl. Phys. B **568**, 367 (2000) [arXiv:hep-ph/9810313].

[59] G. D. Moore and K. Rummukainen, Phys. Rev. **D63** (2001) 045002. [hep-ph/0009132].

[60] Y. Burnier, M. Laine and M. Shaposhnikov, JCAP **0602** (2006) 007 [arXiv:hep-ph/0511246].

[61] G. D. Moore and K. Rummukainen, Phys. Rev. D **61**, 105008 (2000) [arXiv:hep-ph/9906259].

[62] M. Fukugita and T. Yanagida, Phys. Lett. B **174** (1986) 45.

[63] M. A. Luty, Phys. Rev. D **45** (1992) 455.

[64] C. Bonati, M. D'Elia, P. de Forcrand, O. Philipsen and F. Sanfillippo, arXiv:1311.0473 [hep-lat].

[65] E. J. Ferrer, V. de la Incera, C. Manuel, http://www.ice.csic.es/

[66] S. Borsanyi, G. Endrodi, Z. Fodor, A. Jakovac, S. D. Katz, S. Krieg, C. Ratti and K. K. Szabo, JHEP **1011** (2010) 077 [arXiv:1007.2580 [hep-lat]].

[67] "Report of the workshop on BeV/nucleon collisions of heavy ions - how and why", Bear Mountain, New York, Nov. 29 - Dec. 1, 1974. Conf. Proc. C **741017** (1974).

[68] I. Arsene *et al.* [BRAHMS Collaboration], Nucl. Phys. A **757** (2005) 1 [nucl-ex/0410020]. B. B. Back, M. D. Baker, M. Ballintijn, D. S. Barton, B. Becker, R. R. Betts, A. A. Bickley and R. Bindel *et al.*, Nucl. Phys. A **757** (2005) 28 [nucl-ex/0410022]. K. Adcox *et al.* [PHENIX Collaboration], Nucl. Phys. A **757** (2005) 184 [nucl-ex/0410003]. J. Adams *et al.* [STAR Collaboration], Nucl. Phys. A **757** (2005) 102 [nucl-ex/0501009].

[69] J. D. Bjorken, FERMILAB-PUB-82-059-THY.

[70] M. Gyulassy and L. McLerran, Nucl. Phys. A **750** (2005) 30 [nucl-th/0405013].

[71] E. Braaten and A. Nieto, Phys. Rev. Lett. **76** (1996) 1417 [hep-ph/9508406].

[72] M. Laine and Y. Schroder, JHEP **0503** (2005) 067 [hep-ph/0503061].

[73] K. Rummukainen, "$\hat{q}$ from EQCD", XQCD13: Workshop on QCD under extreme conditions. Bern, 5-7 August 2013

[74] S. Caron-Huot, Phys. Rev. D **79**, 065039 (2009) [arXiv:0811.1603 [hep-ph]].

[75] B. G. Zakharov, JETP Lett. **63**, 952 (1996) [hep-ph/9607440]; JETP Lett. **65**, 615 (1997) [hep-ph/9704255].

[76] R. Baier, Y. L. Dokshitzer, S. Peigne and D. Schiff, Phys. Lett. B **345**, 277 (1995) [hep-ph/9411409]. R. Baier, Y. L. Dokshitzer, A. H. Mueller, S. Peigne and D. Schiff, Nucl. Phys. B **483**, 291 (1997) [hep-ph/9607355].

[77] P. B. Arnold, Phys. Rev. D **79** (2009) 065025 [arXiv:0808.2767 [hep-ph]].

[78] P. B. Arnold and W. Xiao, Phys. Rev. D **78** (2008) 125008 [arXiv:0810.1026 [hep-ph]].

[79] M. Panero, K. Rummukainen and A. Schäfer, arXiv:1307.5850 [hep-ph].

[80] S. Nadkarni, Phys. Rev. D **38**, 3287 (1988); N. P. Landsman, Nucl. Phys. B **322**, 498 (1989).

[81] E. Braaten and A. Nieto, Phys. Rev. D **53**, 3421 (1996) [hep-ph/9510408].

[82] K. Kajantie, M. Laine, K. Rummukainen and M. E. Shaposhnikov, Nucl. Phys. B **458**, 90 (1996) [hep-ph/9508379];

[83] G. D. Moore, Nucl. Phys. B **523**, 569 (1998) [hep-lat/9709053].

[84] K. Kajantie, M. Laine, K. Rummukainen and Y. Schroder, Phys. Rev. D **67** (2003) 105008 [hep-ph/0211321].

[85] M. Laine and Y. Schroder, Phys. Rev. D **73** (2006) 085009 [hep-ph/0603048].